Title of the project	Enhanced safety materials for Li-ion batteries
Short title	ENSAMAT
TRL:	1-3
Code:	09I04-03-V02-00028
Beginning of the project:	1.1.2025
Duration:	20 months

Deliverable number	**Deliverable**	**Work package code**	**Entity responsible for deliverable**	**Type**	**Access and dissemination**	**Method of verification**	**Delivery (project implementation month)**
D4.2	**Methodology for monitoring of safety risks**	WP4	SUT	Report	P	Experimental results	M20

Content

_Toc234870620
1. Introduction 3
2. Acoustic defectoscopy 5
3. Strain measurements for battery state and safety risks monitoring 11
3.1 Electrochemical-mechanical modelling and interpretation of surface strain 11
3.2 Surface strain sensing methodology and sensor-position evaluation 13
3.3 Effect of operating conditions and local structural effects 14
3.4. Strain evolution during degradation and battery state prediction 16
_3.5 Conclusion 17
4. EIS for battery state and safety risks monitoring 20
5. AI driven methodology for battery state and safety risks monitoring – internal temperature estimation 30
5.1. Non-Destructive Characterisation via Pulse Response and Impedance 31
5.2. Results 35
5.3. Conclusion 38
6. Summary of results 39

1. Introduction

Within **Work Package 4**, this activity focused on the development and experimental validation of complementary methodologies for monitoring battery state and safety risks using commercially available lithium-ion cells and battery modules. The objective was to establish non-destructive diagnostic approaches capable of providing information about the internal electrochemical, thermal and mechanical condition of batteries, with particular emphasis on parameters relevant to battery safety. Rather than relying on a single sensing principle, the work investigates several complementary methodologies that capture different physical manifestations of battery behaviour and together provide a more comprehensive assessment of battery condition.

The proposed methodologies were experimentally evaluated using commercial lithium-ion pouch cells, cylindrical cells and electric vehicle battery modules. Commercial batteries were intentionally selected because they provide well-characterised and reproducible platforms for validating diagnostic principles before their future application to advanced battery chemistries and safety materials developed within the ENSAMAT project. The knowledge obtained from these studies establishes the methodological basis for future implementation of advanced diagnostics into next-generation battery systems and Battery Management Systems (BMS).

Battery safety is governed by a combination of electrochemical, thermal, mechanical and structural processes that evolve simultaneously during battery operation and ageing. Many hazardous failure mechanisms, including lithium plating, gas generation, electrode cracking, separator deformation, internal short circuits and ultimately thermal runaway, develop progressively inside the cell and cannot be reliably identified using conventional measurements of voltage, current and surface temperature alone. Monitoring additional physical quantities therefore provides valuable information for earlier detection of abnormal operating conditions and more reliable assessment of battery state.

For this reason, the report presents four complementary diagnostic methodologies. **Ultrasonic defectoscopy** investigates changes in acoustic wave propagation to estimate the state of charge and internal temperature while providing sensitivity to structural changes associated with degradation and safety risks. **Surface strain sensing** monitors the mechanical response of the battery casing, enabling assessment of internal stress evolution, electrode expansion and degradation-related mechanical changes. **Electrochemical impedance spectroscopy (EIS)** is used to estimate the internal temperature of battery modules and to improve the reliability of impedance-based state-of-health diagnostics by accounting for thermal effects. Finally, an **AI-driven methodology** combines electrical measurements with

physics-based modelling to estimate internal battery temperature in real time, providing an additional layer for early detection of thermally hazardous operating conditions.

Together, these methodologies form a complementary framework for battery state and safety risk monitoring. While each technique targets different physical phenomena, their combined application provides richer information about the internal condition of lithium-ion batteries and supports the development of future safety-oriented battery management systems capable of earlier fault detection, improved thermal management and enhanced operational reliability.

2. Acoustic defectoscopy

2.1 Acoustic defectoscopy for battery state and safety risks monitoring

Ultrasonic defectoscopy is a non-destructive technique based on the propagation of acoustic waves through a material and across its internal interfaces. A Li-ion cell behaves as a layered composite of tens to hundreds of interfaces, and its mechanical properties - elastic modulus and density - change dynamically as lithium ions intercalate and deintercalate at different states of charge. These changes alter both the speed and the attenuation of a transmitted wave. Their magnitude is governed by the acoustic impedance $Z = \rho c$, where ρ is the material density and c is the local speed of sound. Because the technique probes these structural changes directly, it provides information that complements purely electrical measurements.

Beyond state-of-charge-related changes, ultrasonic defectoscopy is particularly attractive for monitoring battery health and safety because many degradation and failure mechanisms are accompanied by measurable changes in the mechanical structure of the cell. Electrode cracking, delamination, loss of interfacial contact, gas generation, electrolyte depletion, separator deformation, lithium plating, and the onset of internal short circuits all modify the acoustic propagation path, resulting in changes in wave velocity, attenuation, reflection, and frequency response. These acoustic signatures often emerge before significant electrical performance degradation becomes apparent, enabling earlier detection of abnormal conditions.

Methodology

The acoustic signal A-scan - amplitude as a function of Time-of-Flight (ToF) - was acquired with a SIUI SyncScan TOFD instrument using 5 MHz, 6 mm probes at a receive gain of 60.5 dB and was synchronized with electrical data from a Neware cycler. The principal test cells were Melasta SLPB6945135HW Li-polymer pouch cells. Two experiments were performed on them. First isolated the effect of SOC at a fixed 23 °C room temperature, and the second repeated the charge cycle inside a temperature-controlled chamber at 15 °C, 20 °C, and 25 °C. For consistency, only the charging part of each cycle was analyzed, because the cell temperature is more stable during charge than during the 7.8 A discharge. The same method was then applied to a commercial cylindrical cell, Panasonic NCR18650B (18650 format, NCA/graphite chemistry) - to verify that the SOC dependence generalizes beyond the pouch format and to relate the acoustic signal directly to the cell's electrochemistry.

Estimation of SoC

Figure 2.1 shows the transmitted A-scan at 0 %, 50 %, and 100 % SOC. As the cell charges, the peaks grow in amplitude - indicating better sound transmission and lower losses - and shift slightly in ToF. Peaks and valleys are numbered from left to right: peak no. 3 and valley no. 17

were selected as the most representative features. For peak no. 3 the amplitude rose from 31 % at 0 % SOC to 95 % at 100 % SOC, whereas its ToF moved only 0.049 µs. For valley no. 17 the opposite holds - the ToF shift dominates (≈0.195 µs) while the amplitude changes by only about 2 %.

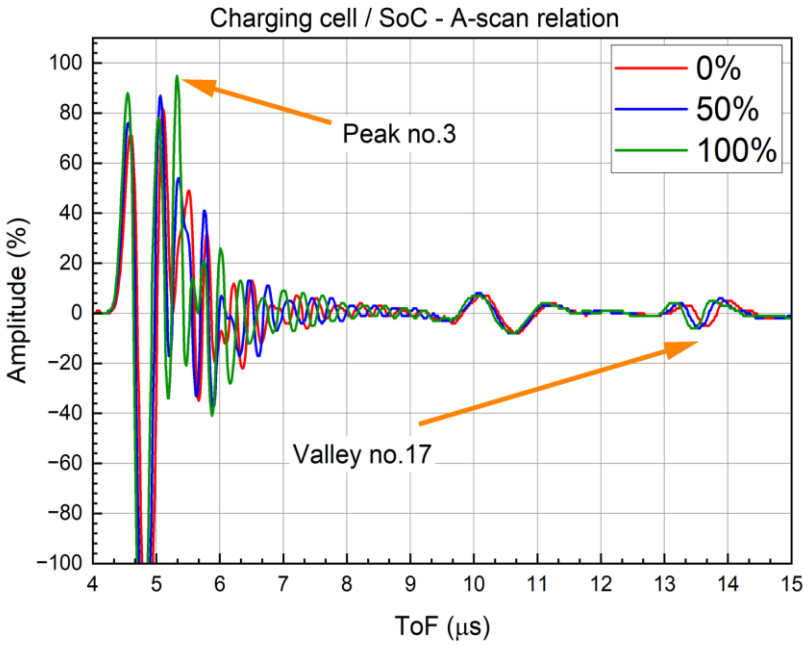
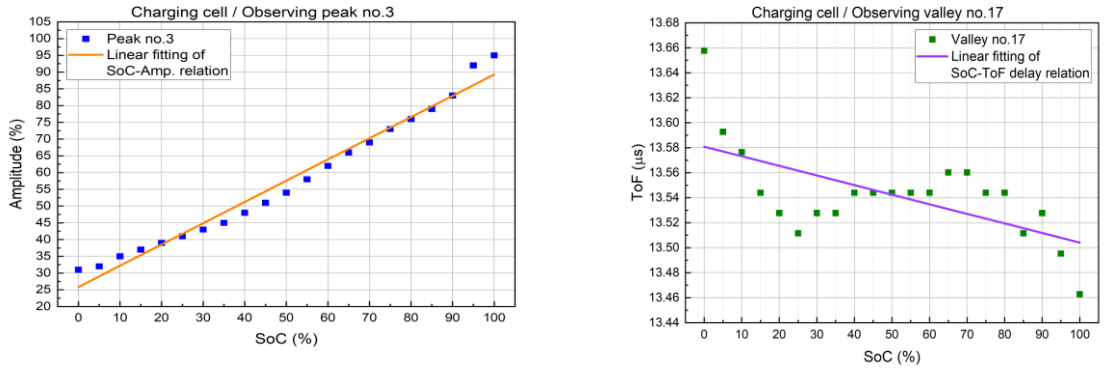


Figure 2.1: *Transmitted A-scans of the cell at 0 %, 50 % and 100 % SOC, with peak no. 3 and valley no. 17 highlighted (orange arrows mark the shift direction).*

Tracking these two features across the whole charge produces the curves in Figure 2.2. The peak no. 3 amplitude (Figure 2.2a) increases quasi-linearly with SOC. Linear fit $y = a + b \cdot x$ gives a slope of 0.634 ± 0.022 with close agreement to the data. The valley no. 17 ToF (Figure 2.2b) also trends downward with SOC but is markedly less monotonic - between roughly 25 % and 70 % SOC the curve is non-monotonic, while the first ~25 % and last ~30 % are quasi-linear. This confirms that **amplitude, not ToF, is the more reliable observable for SOC**, consistent with the known higher sensitivity of cells near the 0 % and 100 % SOC limits. Physically, the rising amplitude reflects the stiffening of the graphite anode as it becomes progressively lithiated during charging. Increasing elastic modulus raises the acoustic impedance of the electrode stack and reduces transmission losses, so more energy reaches the receiving probe.



a) **b)**

Figure 2.2: *SOC dependence on the two representative features.* ***a)*** *Amplitude of peak no. 3 versus SOC, with linear fit (slope 0.634 ± 0.022).* ***b)*** *ToF of valley no. 17 versus SOC with its linear fit.*

Influence of temperature on the SoC estimation

The second experiment repeated the charge cycle at 15 °C, 20 °C, and 25 °C. Figure 2.3 shows the corresponding A-scans at a constant 100 % SOC. Here the dominant change is in ToF rather than amplitude: between 15 °C and 25 °C the studied valleys shifted by about 0.31 µs while their amplitude changed by only ~1 %. A colder cell transmits sound faster, so the whole A-scan moves toward the time axis as temperature drops.

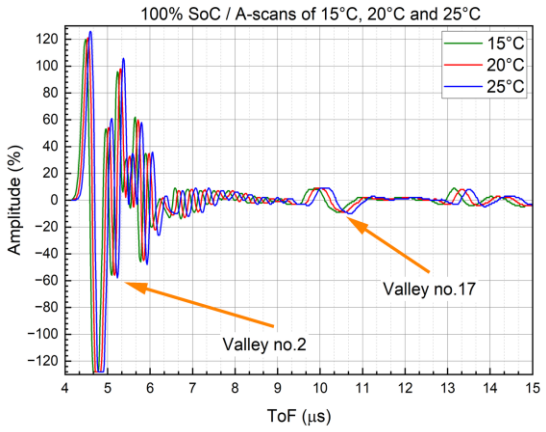


Figure 2.3: *Transmitted A-scans at a constant 100 % SOC for chamber temperatures of 15 °C, 20 °C and 25 °C, with valley no. 2 and valley no. 17 highlighted.*

Plotting the two features against SOC for all three temperatures separates the SOC and temperature contributions. The amplitude of valley no. 2 (Figure 2.4a) follows essentially the same SOC trend at every temperature. Three datasets overlap, with a common slope of −0.524 ± 0.017 - showing that the amplitude-SOC relationship is largely temperature-independent. By contrast, the ToF of valley no. 17 (Figure 2.4b) is split into three clearly separated curves, one per temperature, with a near-constant vertical offset of roughly 0.16 µs per 5 °C. Within each temperature the ToF–SOC slope is small and stable (for example -0.00186 ± 1.8×10^{-4} at 15 °C). The per-point error of this ToF fit stayed below ~0.35 %, which is low because the ToF is measured in hundreds of microseconds.

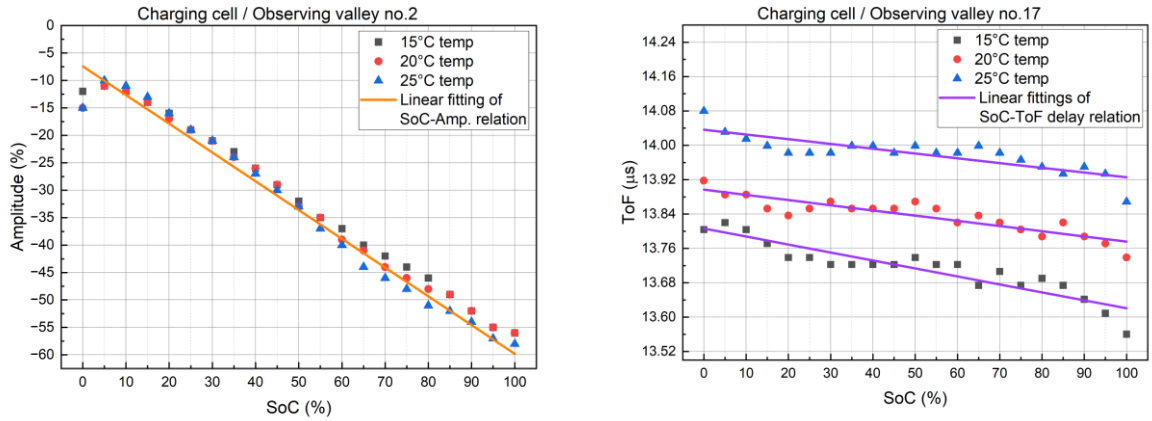


Figure 2.4: *Charge cycles at three temperatures.* ***a)*** *amplitude of valley no. 2 versus SOC - the curves overlap, confirming a temperature-independent SOC response.* ***b)*** *ToF of valley no. 17 versus SOC with linear fits, separated by a near-constant offset per temperature step.*

This behaviour has a direct practical consequence. Because the transmitted amplitude reports SOC almost independently of temperature, while the ToF reports temperature with only a weak dependence on SOC, the two readings can be combined. Measured ToF can be used to estimate and compensate the temperature contribution to the acoustic signal, leaving a cleaner amplitude-based SOC estimate even when the cell is not held at a fixed temperature. Since the speed of sound is strongly temperature dependent, the measured ToF can also be directly exploited to estimate the internal temperature of the cell in real time, providing valuable information that is difficult to obtain from conventional surface-mounted temperature sensors. This capability is particularly important for battery safety monitoring, as local temperature gradients and internal hot spots often precede abnormal degradation and thermal runaway. Consequently, ultrasonic measurements provide simultaneous information on both the electrochemical and thermal state of the cell, increasing the robustness of state estimation and enabling earlier detection of safety-critical conditions. Establishing what the acoustic signal tracks at the electrochemical level is the natural next step and is examined below using a cylindrical cell.

Extension to a cylindrical cell and acoustic - electrochemical correlation

To test whether the SOC dependence generalizes beyond the pouch format and to relate the acoustic signal directly to the cell's electrochemistry, the same through-transmission method was applied to a commercial cylindrical cell - Panasonic NCR18650B (18650 format, NCA/graphite chemistry). Here the transmitted signal was acquired continuously as a B-scan - amplitude as a function of position along the cell and experiment time - and synchronized with the electrochemical cycling data over a slow quasi-equilibrium (open-circuit-voltage, OCV) discharge and a pulsed charge. The raw B-scan (Figure 2.5a) and its Hilbert envelope (Figure 2.5b) both reveal a clear and repeatable evolution of the transmitted amplitude and time-of-flight with SOC. As in the pouch cell, the response is non-monotonic across the charge-discharge range.

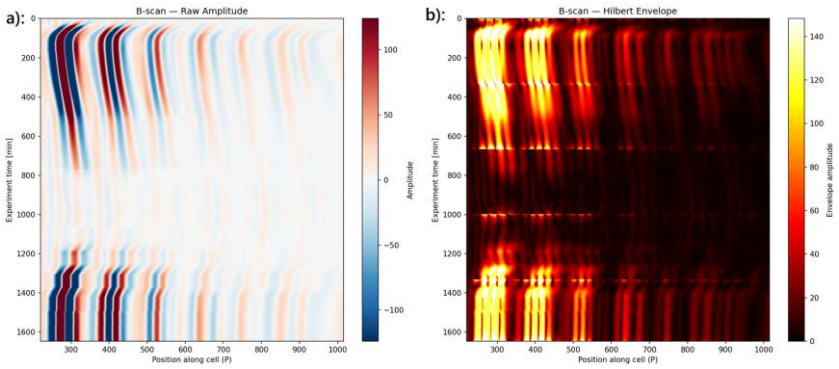


Figure 2.5: *Acoustic through-transmission B-scan of the Panasonic NCR18650B cell over a slow quasi-equilibrium (OCV) discharge and pulsed charge.* ***a)*** *raw transmitted-signal amplitude versus position along the cell and experiment time;* ***b)*** *Hilbert envelope of the same dataset, showing the evolution of the transmitted signal with SOC.*

Because the acoustic and electrochemical data were recorded in the same experiment, the acoustic features can be compared directly with an incremental capacity analysis (ICA, −dQ/dV) of the discharge. Figure 2.6a shows the −dQ/dV curve against cell voltage. Overlaying these on the tracked acoustic envelope peaks A and B as functions of SOC (Figure 2.6b) shows that the acoustic features move in step with the electrochemical signatures. Building on this, ongoing work extends the approach to cells aged under controlled conditions, to identify acoustic markers of distinct degradation mechanisms.

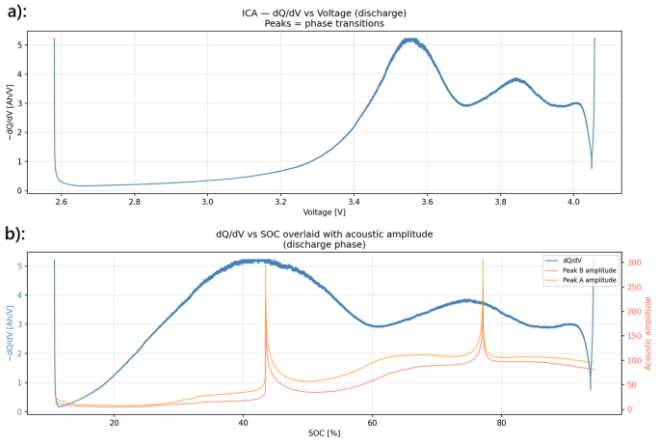


Figure 2.6: *Acoustic - electrochemical correlation for the NCR18650B cell.* ***a)*** *Incremental capacity analysis (−dQ/dV) versus cell voltage during the slow (OCV) discharge.* ***b)*** *−dQ/dV and the tracked acoustic envelope amplitude (peaks A and B) versus SOC, showing the signs of dependence between electrochemical and acoustic features.*

2.2 Conclusion

Taken together, these measurements show that through-transmission ultrasonic defectoscopy resolves both the State of Charge and the temperature of a Li-ion cell, with the two effects mapping onto largely independent signal features: the transmitted amplitude tracks SOC quasi-linearly (Melasta pouch, peak no. 3 slope 0.634 ± 0.022) and is essentially insensitive to temperature, while the time-of-flight tracks temperature with only a weak SOC dependence.

This enables simultaneous estimation of the electrochemical and thermal state of the battery using a single sensing modality, with ToF serving as an acoustic estimator of the internal cell temperature. Extending the method to a cylindrical Panasonic NCR18650B confirmed that the SOC dependence generalizes across formats, and acquiring the acoustic and electrochemical data together showed the acoustic envelope features moving in step with the incremental-capacity (dQ/dV) signatures of the graphite phase transitions. The transmitted signal therefore carries genuine state-resolved information about the electrode stack, providing the basis for degradation diagnostics, State-of-Health estimation, and early detection of safety-critical conditions. By combining amplitude- and ToF-based features, ultrasonic defectoscopy offers a powerful framework for real-time battery monitoring, enabling improved state estimation, thermal management, and early warning of abnormal processes that may precede thermal runaway.

3. Strain measurements for battery state and safety risks monitoring

This chapter summarizes the electrochemical-mechanical analysis and experimental surface strain sensing of cylindrical lithium-ion cells with silicon-containing anodes. The work focuses on the use of surface strain as a complementary diagnostic signal for battery state estimation, safety risk monitoring, degradation diagnostics, and prediction of abnormal operating conditions. By directly tracking the mechanical response of the cell during electrochemical cycling, strain measurements provide valuable information on internal processes that cannot be captured by electrical measurements alone, supporting the development of more reliable battery management systems and future safety-oriented control strategies. The report is based on numerical simulations performed in COMSOL Multiphysics and on experimental measurements of Molicel INR21700-P45B and INR21700-M35A cells equipped with externally bonded strain gauges.

3.1 Electrochemical-mechanical modelling and interpretation of surface strain

Mechanism of strain generation in SiG-based cells

The mechanical response of a lithium-ion battery originates mainly from volume changes of active materials during lithiation and delithiation. During charging, lithium ions are inserted into the anode material, causing its expansion. During discharge, the opposite process occurs and part of the volume change is reversed. At the level of a cylindrical cell, these cyclic volume changes can be transferred through the internal structure to the metallic casing and observed as measurable surface strain or deformation. In silicon-graphite composite anodes, this effect is amplified by the presence of silicon. Silicon offers high theoretical capacity, but it can undergo a volume change of approximately 250-300% during lithiation and delithiation. Such deformation induces diffusion-driven mechanical stress, particle cracking and pulverization, loss of electrical contact and repeated formation of the solid-electrolyte interphase (SEI). As a result, the mechanical response of the cell does not reflect only the instantaneous state of charge, but may also contain information about progressive degradation of the active material.

Numerical analysis of silicon particle size and mechanical stress

To complement the experimental measurements, a numerical analysis of the electrochemical-mechanical cell response was performed in COMSOL Multiphysics using the Heterogeneous Lithium-Ion Battery model. The analysis focused on the influence of silicon particle size in the anode on the evolution of internal mechanical stress during charging. Simulations were carried out during 1C charging for silicon particle sizes from 0.666×10^{-6}m to 1.963×10^{-6}m.

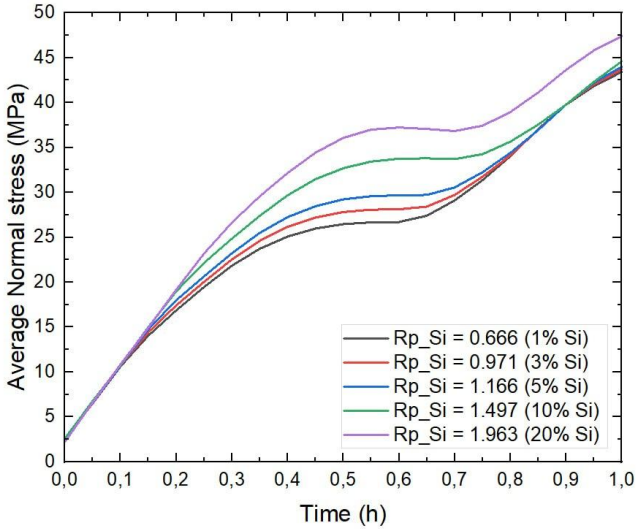


Figure 3.1: *Simulated time evolution of internal average normal mechanical stress during 1C charging for silicon particle sizes from 0.666 x 10^{-6} m to 1.963 x 10^{-6} m.*

The simulation results indicate that the larger silicon particle size of 1.963 x 10^{-6} m leads to higher internal mechanical stress during most of the charging process compared with the 0.666 x 10^{-6} m case. This confirms that particle-level design parameters can influence the intensity of lithiation-induced mechanical loading and can therefore affect the mechanical response observed at the cell level.

The modelling was also used to compare the simulated voltage response with mechanical deformation coupling. This comparison helps clarify whether deformation terms affect the electrochemical response predicted by the model and provides additional support for the interpretation of experimentally measured strain signals.

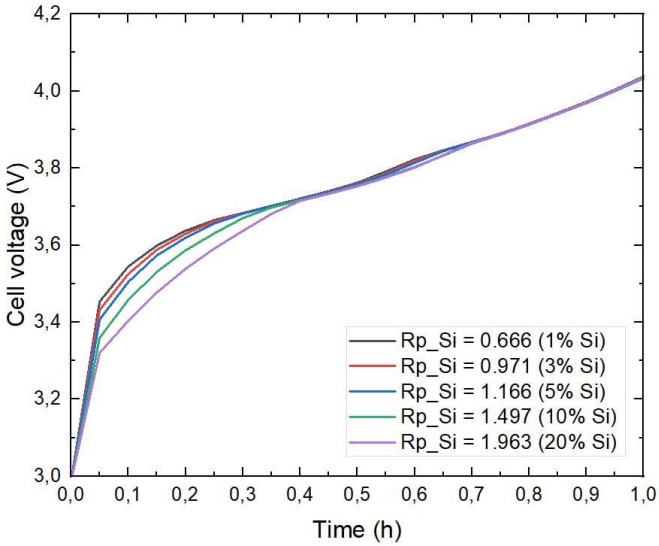


Figure 3.2*: Comparison of the simulated cell voltage response during 1C charging with considering mechanical deformation.*

The voltage profiles show only a moderate difference, mainly in the early stage of charging. Nevertheless, the comparison confirms that electrochemical and mechanical processes are

coupled in silicon-containing anodes, and that deformation can influence the predicted cell response. These numerical results establish a physical link between anode expansion, internal mechanical stress and measurable surface strain.

3.2 Surface strain sensing methodology and sensor-position evaluation

Experimental measurement setup

Surface strain measurements were performed on cylindrical lithium-ion cells, where strain gauges were attached directly to the outer metallic casing of the cell. The aim of the measurement was to record changes in surface strain during charging, discharging and long-term cycling. This configuration enables non-invasive monitoring of the mechanical response without modifying the internal cell structure.

The experimental measurements were performed on Molicel INR21700-P45B and Molicel INR21700-M35A cylindrical cells. An OMEGA KFH-10-120-C1-11L1M2R strain gauge was attached to the cell surface using a thin layer of epoxy adhesive. The strain gauge had a resistance of 120.4 Ohm +/- 0.35%, gauge factor 2.15 +/- 1%, grid length 10 mm, grid width 3 mm and operating temperature range from -10 degC to 155 degC. A Keysight DAQ973A data acquisition system with a DAQM901A module was used for sensor excitation and data acquisition.

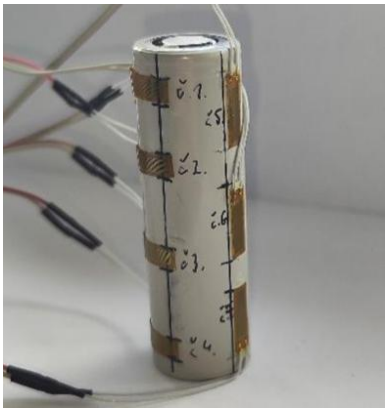


Figure 3.3: *Placement of strain gauges on the Molicel INR21700-P45B cell surface to determine a suitable position for surface strain measurement.*

Sensor placement and data acquisition

The placement of the strain gauge is critical for cylindrical cells because surface strain may not be uniform along the circumference or height of the cell. The internal arrangement of the jelly roll, the contact between the jelly-roll structure and the metallic casing, and the exact sensor position can significantly affect the sign, amplitude and shape of the measured signal. For this reason, several sensor positions were evaluated in order to identify locations with strong and reproducible mechanical response.

The recorded strain signal was evaluated together with electrical and thermal quantities, especially voltage, current, temperature, state of charge (SoC) and cycle number. The Neware

battery cycler data were synchronized with the Keysight DAQ973A strain measurements. After synchronization, dependencies of surface strain on SoC and temperature were obtained for each sensor position.

Since individual strain gauges can exhibit different absolute signal levels, their outputs were normalized before comparison. The normalized strain was calculated as epsilon_norm = (epsilon - epsilon_min) / (epsilon_max - epsilon_min). Strain sensitivity was then evaluated with respect to SoC and temperature using numerical derivatives of the normalized signal. This allowed quantitative comparison of which sensor position provides the most pronounced response to electrochemical and thermal changes.

Evaluation of sensor position

The comparison of sensor positions showed that the mechanical response on the cell surface is not spatially homogeneous. The highest cumulative sensitivity to SoC changes was obtained for sensors No. 2 and No. 3, reaching 16.669 microstrain per 1% SoC and 16.760 microstrain per 1% SoC, respectively. For comparison, sensors No. 5 and No. 6 reached lower cumulative values of 8.956 and 10.218 microstrain per 1% SoC.

A similar trend was observed for temperature sensitivity. Sensors No. 2 and No. 3 reached cumulative values of 3.122 and 3.178 microstrain per 1 degC, while sensors No. 5 and No. 6 reached 1.654 and 1.810 microstrain per 1 degC. Based on these results, the positions corresponding to sensors No. 2 and No. 3 were identified as the most suitable locations for further measurements and analysis. This suggests that the central region of the cylindrical cell provides the most pronounced surface strain response.

Table 1: Selected sensor-position sensitivity values

Sensor position	SoC sensitivity (microstrain / 1% SoC)	Temperature sensitivity (microstrain / 1 degC)
No. 2	16.669	3.122
No. 3	16.760	3.178
No. 5	8.956	1.654
No. 6	10.218	1.810

3.3 Effect of operating conditions and local structural effects

Effect of C-rate on surface strain response

After selecting suitable sensor positions, the influence of current load on surface strain response was evaluated. Strain profiles were compared during charging and discharging at different C-rates. At lower current loads, the surface strain changed more smoothly and followed the SoC evolution more gradually. With increasing C-rate, the slope and shape of the

strain curve changed, indicating a stronger influence of dynamic electrochemical-mechanical processes inside the cell.

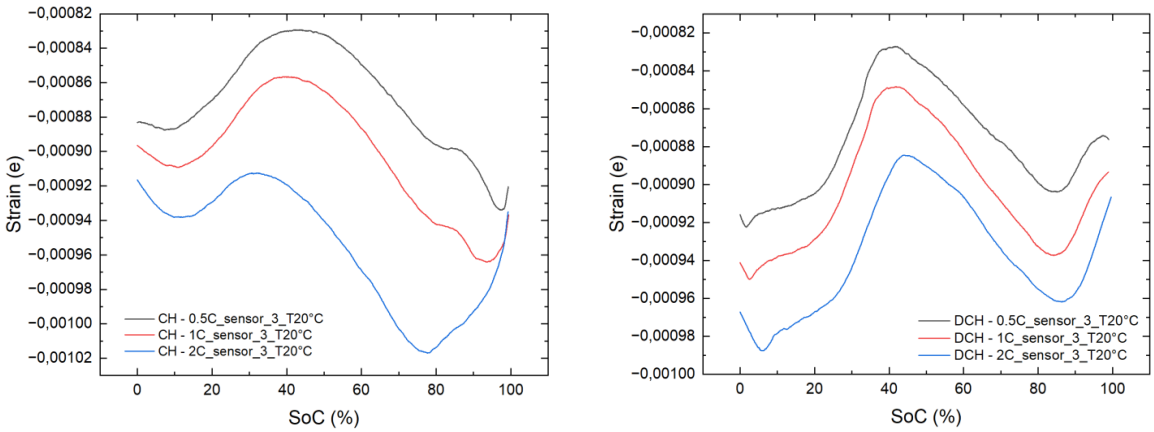


Figure 3.4: *Effect of C-rate on surface strain during charging and discharging for a representative strain-gauge position.*

The curves for different C-rates are shifted relative to each other, which indicates that current regimes can be distinguished from the strain response. The differences are particularly visible at higher SoC and under higher-current operation. The comparison between charging and discharging also shows that the mechanical response is not simply the same curve in the opposite direction, it depends on SoC, current load and cycling direction.

Temperature-dependent strain response

The temperature dependence of surface strain was evaluated by comparing strain profiles at 10 °C and 20 °C for charging currents of 0.5C, 1C and 2C. At the low charging current of 0.5C, the curves measured at both temperatures had a similar shape and differed mainly by a vertical shift. This shift is consistent with temperature-dependent behaviour of both the battery cell and the strain gauge.

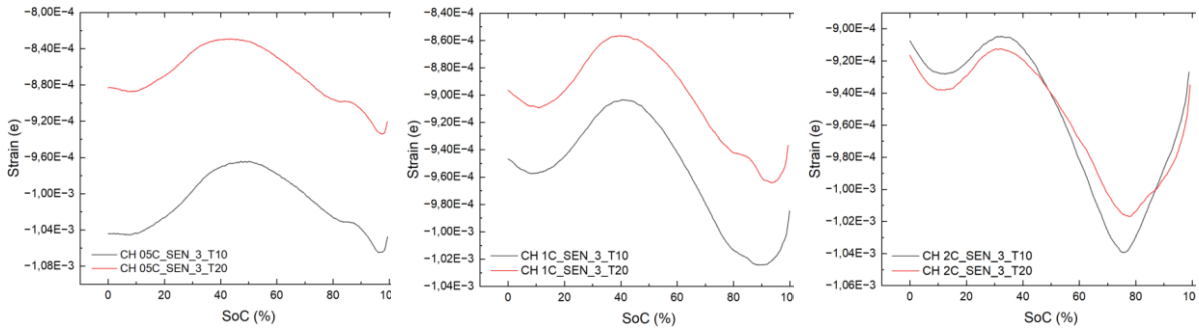


Figure 3.5: *Strain dependence on SoC at 10 °C and 20 °C for strain gauge No. 3 during charging at 0.5C, 1C and 2C.*

At higher C-rates, the curves measured at 10 °C and 20 °C moved closer and could intersect in some SoC regions. This shows that the strain signal is influenced not only by temperature, but also by current-induced effects such as polarization, concentration gradients, heat generation and non-uniform lithium distribution in active materials. For high-current regimes,

surface strain must therefore be interpreted as a coupled electrochemical, thermal and mechanical response.

Local anomalies in strain responses and CT interpretation

In addition to the main surface strain trend, a secondary local peak was identified in the strain profiles. This feature was most pronounced at lower charging currents, where the strain response was less affected by dynamic effects associated with higher current loading. At higher currents, the secondary peak was mainly visible at elevated temperature, while in the 2C regime its identification became significantly more difficult.

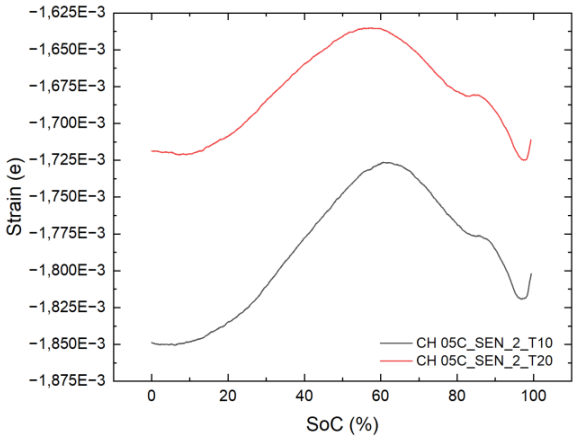


Figure 3.6: *Detail of the surface strain profile with the marked secondary local peak.*

The occurrence of the secondary peak shows that temperature and C-rate affect not only strain amplitude but also the shape of the strain curve itself. CT analysis of a cell of the same type revealed local structural imperfections, especially layer separations and winding defects. These inhomogeneities may affect the local transfer of mechanical response from the internal cell structure to the metallic casing and provide a plausible explanation for deviations observed in the strain signal.

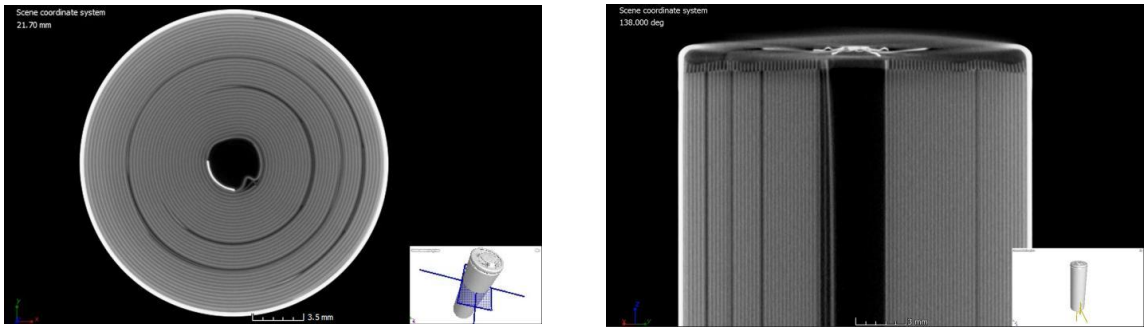


Figure 3.7: *CT scan of the battery internal winding and negative terminal region, showing local structural features relevant to interpretation of strain anomalies.*

3.4. Strain evolution during degradation and battery state prediction

Long-term strain response during degradation

To evaluate the applicability of surface strain for degradation monitoring, long-term measurements of Molicel INR21700-M35A cells were analysed. These cells were selected mainly due to their lower nominal capacity compared to INR21700-P45B cells, which enabled higher relative current loading within the available limits of the measurement setup. This made it possible to accelerate degradation processes during cycling and observe how the mechanical response changes with progressive aging.

For degradation analysis, strain profiles obtained during the charging branch of the open-circuit-voltage characterization procedure (OCV_CH) were compared. In this mode, changes in strain can be monitored more accurately due to the use of low C-rate values. For easier comparison, selected strain profiles were multiplied by -1, therefore a shift of the curves toward higher values on the y-axis corresponds to a decrease in the original strain value.

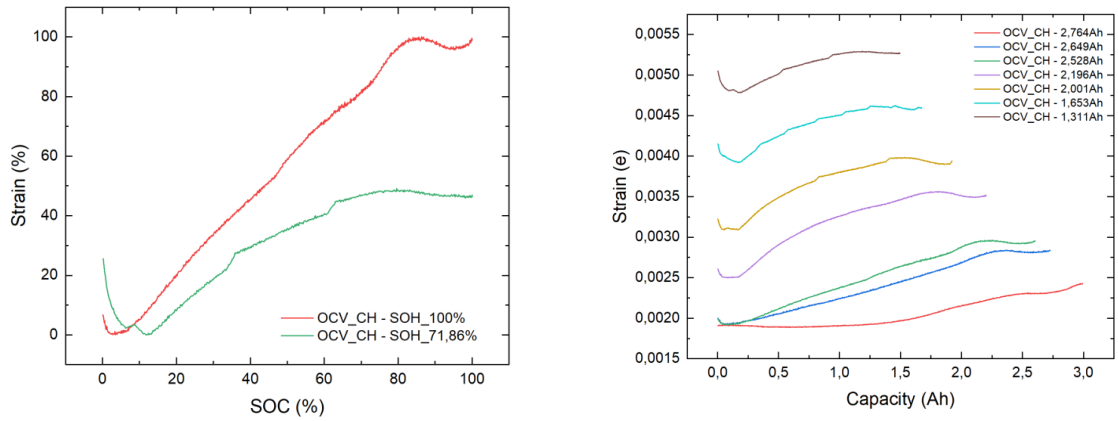


***Figure 3.8**: Degradation-related changes in the surface strain response: normalized OCV charging comparison at different SoH levels and shift of strain profiles with decreasing usable capacity.*

The strain profiles gradually shifted with decreasing usable cell capacity. Curves corresponding to higher capacities, such as 2.764 Ah and 2.649 Ah, were located at lower values of the transformed signal, while a degraded profile at 1.311 Ah shifted significantly upward. Considering the sign transformation, this corresponds to a decrease in the original strain signal. This result shows that degradation is reflected not only by a change in strain amplitude, but also by a shift in the baseline level of the mechanical response.

An additional comparison of normalized profiles at SoH = 100% and SoH = 71.86% showed a significant reduction in mechanical response after degradation. In the initial state, normalized strain reached values close to 100% at high SoC levels, whereas at SoH = 71.86% it reached only approximately 45-50%. This decrease confirms the reduction of mechanical response amplitude and the change in the volumetric response of active materials during aging.

3.5 Conclusion

The work presented in this report focuses on the use of surface strain as a complementary diagnostic signal for cylindrical lithium-ion cells with silicon-containing anodes. Numerical

modelling, experimental strain-gauge measurements and degradation analysis were combined to evaluate the relationship between electrochemical operation, mechanical stress and surface strain response.

- Electrochemical-mechanical simulations showed that the silicon particle size influences the development of internal mechanical stress during 1C charging. The larger particle size 1.963×10^{-6} m produced higher stress than the 0.666×10^{-6} m case during most of the charging process, confirming that electrode design parameters directly affect the mechanical loading of the cell and may influence its long-term reliability and safety.
- Comparison of simulated voltage response with deformation coupling confirmed that mechanical deformation can slightly affect the modelled electrochemical response, particularly in the early stage of charging, demonstrating the coupled nature of electrochemical and mechanical processes.
- The experimental methodology enabled non-invasive surface strain measurement on commercial Molicel INR21700-P45B and INR21700-M35A cylindrical cells using OMEGA strain gauges bonded to the external metallic casing.
- Sensor-position evaluation showed that the surface strain response is spatially non-uniform. Sensors No. 2 and No. 3 achieved the highest cumulative sensitivity to SoC and temperature and were therefore selected as the most suitable positions for further analysis.
- The C-rate study demonstrated that surface strain curves shift and change shape with current load. The response differs between charging and discharging, indicating that strain depends not only on SoC but also on current regime and cycling direction. These changes reflect variations in internal electrochemical-mechanical behaviour associated with increased polarization, heat generation and non-uniform lithium distribution under demanding operating conditions.
- Temperature-dependent measurements at 10 °C and 20 °C showed that at low C-rate the main difference is a vertical curve shift, while at higher C-rates the curves converge or intersect due to coupled thermal, electrochemical and mechanical effects.
- A secondary local peak was identified in the strain response. CT analysis revealed local structural imperfections such as layer separations and winding defects, which may influence the transfer of internal deformation to the outer casing. This demonstrates that strain sensing is sensitive to local structural inhomogeneities and may therefore contribute to the early identification of mechanically abnormal cells.
- Long-term measurements of Molicel INR21700-M35A cells showed degradation-related changes in strain profiles. With capacity loss, strain profiles shifted and the

maximum normalized response decreased from approximately 100% at SoH = 100% to 45–50% at SoH = 71.86%, indicating that progressive ageing is accompanied by a measurable reduction in the mechanical response of the cell.

The obtained results demonstrate that surface strain contains valuable information not only for battery state estimation but also for degradation diagnostics and safety risk monitoring. Deviations from the expected strain behaviour can indicate increasing mechanical instability associated with phenomena such as particle cracking, loss of interfacial contact, structural inhomogeneities or non-uniform lithiation, which may precede severe failure mechanisms. Consequently, surface strain sensing represents a promising complementary input for future battery management systems, enabling more robust battery state estimation, early fault detection, safety-oriented control strategies and adaptive charging methods aimed at extending battery lifetime while reducing the risk of hazardous operating conditions.

4. EIS for battery state and safety risks monitoring

Electrochemical impedance spectroscopy (EIS) is increasingly recognized as a powerful non-invasive diagnostic technique capable of monitoring both battery state and safety-related parameters. Unlike conventional electrical measurements, EIS provides insight into the internal electrochemical processes governing charge transfer, ion transport and diffusion, all of which are strongly influenced by the operating condition of the battery. Since impedance characteristics are highly sensitive to temperature, EIS can also be exploited for indirect monitoring of the internal thermal state of a battery. This capability is particularly important for battery safety, as excessive internal temperature and localized overheating are among the primary factors accelerating degradation and increasing the risk of thermal runaway. Consequently, EIS-based internal temperature estimation represents a promising approach for safety-oriented battery management systems, enabling earlier detection of abnormal thermal conditions without the need for intrusive sensors.

4.1. Monitoring of internal temperature

This chapter summarizes the investigation of EIS-based internal temperature estimation as a tool for battery state and safety risk monitoring. Particular attention is given to identifying impedance features that reliably track the internal temperature of aged EV battery modules and can therefore support thermal management, early identification of abnormal thermal behaviour, and safety-oriented battery management in both first-life EV operation and second-life stationary energy storage applications.

Methodology

The experiment was performed on a used 24 kWh Nissan Leaf battery module with a 2S2P configuration. For EIS measurements, one 2S1P sub-module was used. The module had a state of health of approximately 85%. The cells contained $LiMn_2O_4$ with $LiNiO_2$ as the cathode and graphite as the anode, with a nominal capacity of 66.2 Ah at a 0.3C rate. Before the main experiment, the module was conditioned by repeated charge–discharge cycling at 25 °C. It was then discharged to SOC 50% and allowed to relax for 24 hours. A set of repeated EIS measurements was used to determine the most suitable regularisation parameter for DRT calculation. All impedance measurements were performed galvanostatically in the frequency range from 1 kHz to 10 mHz.

The main experiment was conducted at temperatures from 50 °C to 0 °C in 10 °C increments and at SOC levels from 90% to 10% in 10% increments. At each temperature, the module was allowed to relax for 5 hours to ensure that the internal temperature reached the chamber temperature. The module was then discharged stepwise to the desired SOC levels using a low current, followed by relaxation and EIS measurement at each SOC. The measured EIS spectra were analysed using two approaches. First, an equivalent circuit model was fitted to the data

to obtain individual ECM parameters. Second, DRT analysis was performed using standard Tikhonov regularisation to identify individual time-domain features and evaluate their temperature dependence (Figure 4.1).

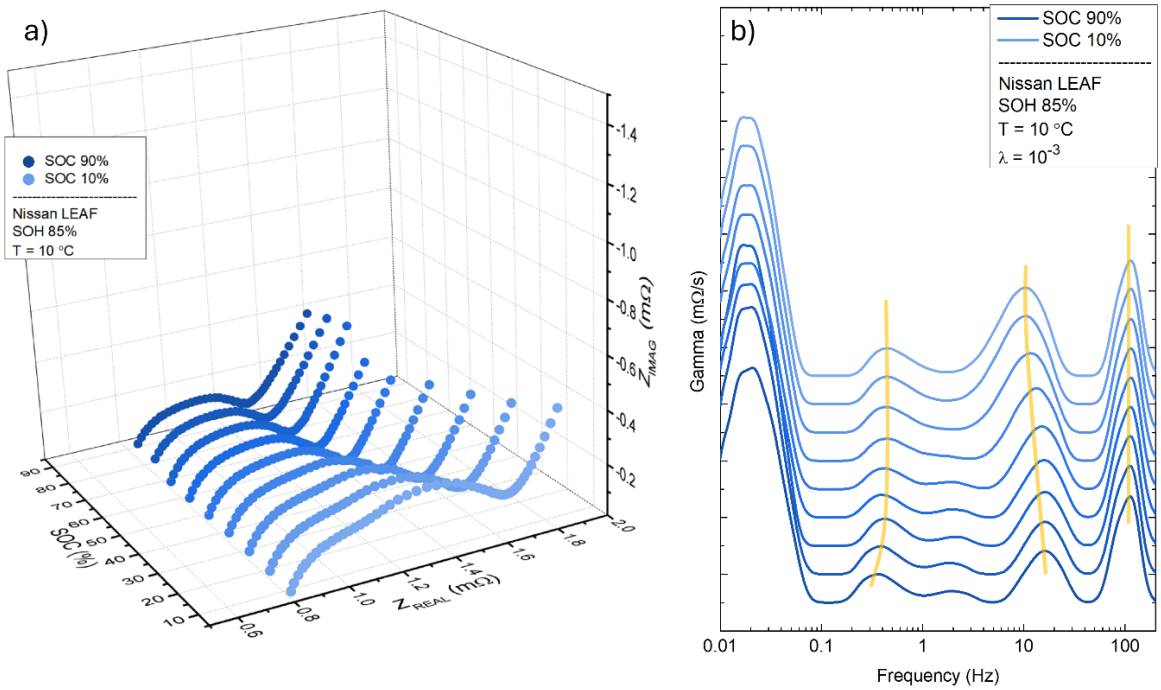


Figure 4.1: *a) Representative Nyquist plots and b) distribution of relaxation times for selected temperature of -10°C.*

DRT Regularisation Parameter

Since DRT analysis strongly depends on the choice of the regularisation parameter, several values were tested using repeated EIS measurements performed at SOC 50% and 25 °C. The DRT curves were calculated using λ values from 10^{-1} to 10^{-4}. Higher values led to under-interpretation of the system, while the lowest tested value produced excessive variation between repeated curves, indicating over-interpretation and sensitivity to noise. The most suitable value was found to be $\lambda = 10^{-3}$. This value provided four distinct and stable DRT peaks without introducing excessive variance between repeated measurements. Therefore, $\lambda = 10^{-3}$ was used for all subsequent DRT calculations in this study.

Temperature Dependence of ECM Parameters

The EIS spectra measured at different temperatures showed a clear increase in both real and imaginary impedance values with decreasing temperature. The Nyquist plots consisted of an induction tail, two depressed semicircles and a diffusion tail (Figure 4.2). Based on these features, an equivalent circuit model was constructed, including an inductive high-frequency contribution, ohmic resistance, double-layer resistance, charge-transfer resistance and a Warburg diffusion element. The results of the EIS data fitting are displayed in Figure 4.3.

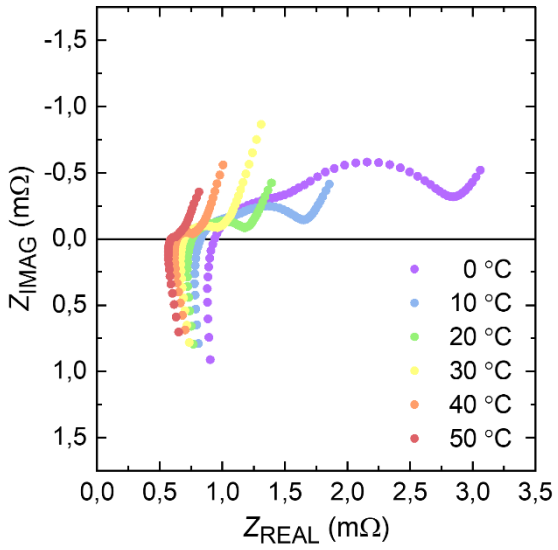


Figure 4.2: *Nyquist plots obtained at various temperatures.*

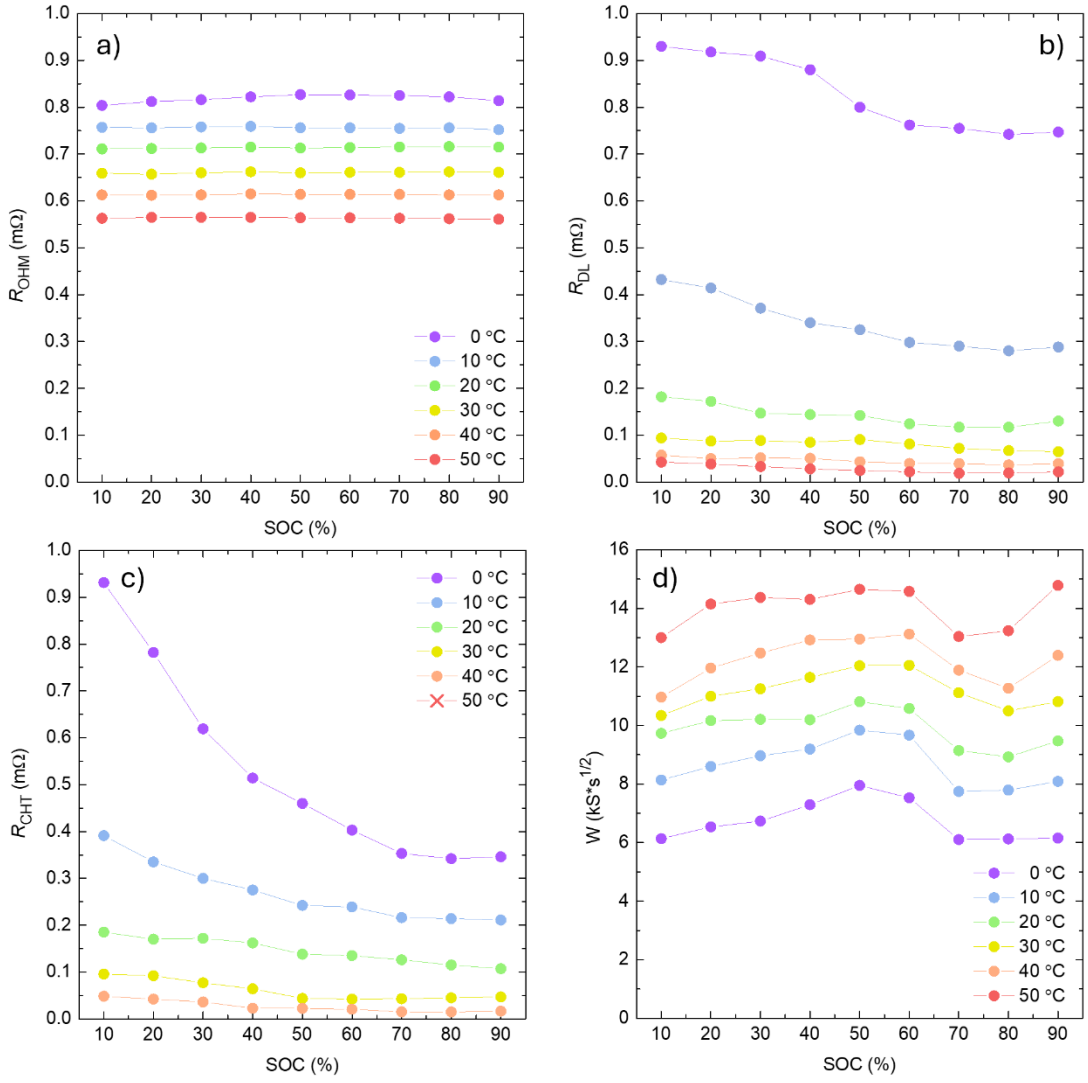


Figure 4.3: *Results of the EIS data fitting, where a) represents ohmic resistance, b) resistance of the double-layer (or SEI layer resistance), c) charge-transfer resistance, and d) represents values of Warburg element.*

The fitted ECM parameters showed different levels of suitability for determining the internal temperature (Figure 4.4). The high-frequency inductive resistance R_0 increased with decreasing temperature, but its behaviour was not sufficiently consistent, particularly at elevated temperatures. Therefore, R_0 was not considered suitable for reliable temperature determination. The ohmic resistance R_{OHM} showed almost no SOC dependence and a clear temperature dependence. This made it one of the most promising ECM-based indicators of internal temperature. Charge-transfer resistance R_{CHT} also showed usable temperature-dependent behaviour, although it had stronger SOC dependence. In contrast, the double-layer resistance R_{DL} was unsuitable because the corresponding feature disappeared at 50 °C. The Warburg element also showed temperature dependence, but the resulting deviations were too high for accurate temperature determination. The calculated temperature deviations confirmed that R_{OHM} and R_{CHT} provided the best ECM-based accuracy. However, both parameters are strongly affected by ageing and degradation. R_{OHM} may change due to electrolyte degradation, while R_{CHT} is sensitive to loss of lithium inventory, SEI growth and particle cracking. Therefore, using these ECM parameters in real-world applications would require a complex database covering different temperatures, SOC levels and degradation states. This limits their practical applicability for reliable internal temperature determination.

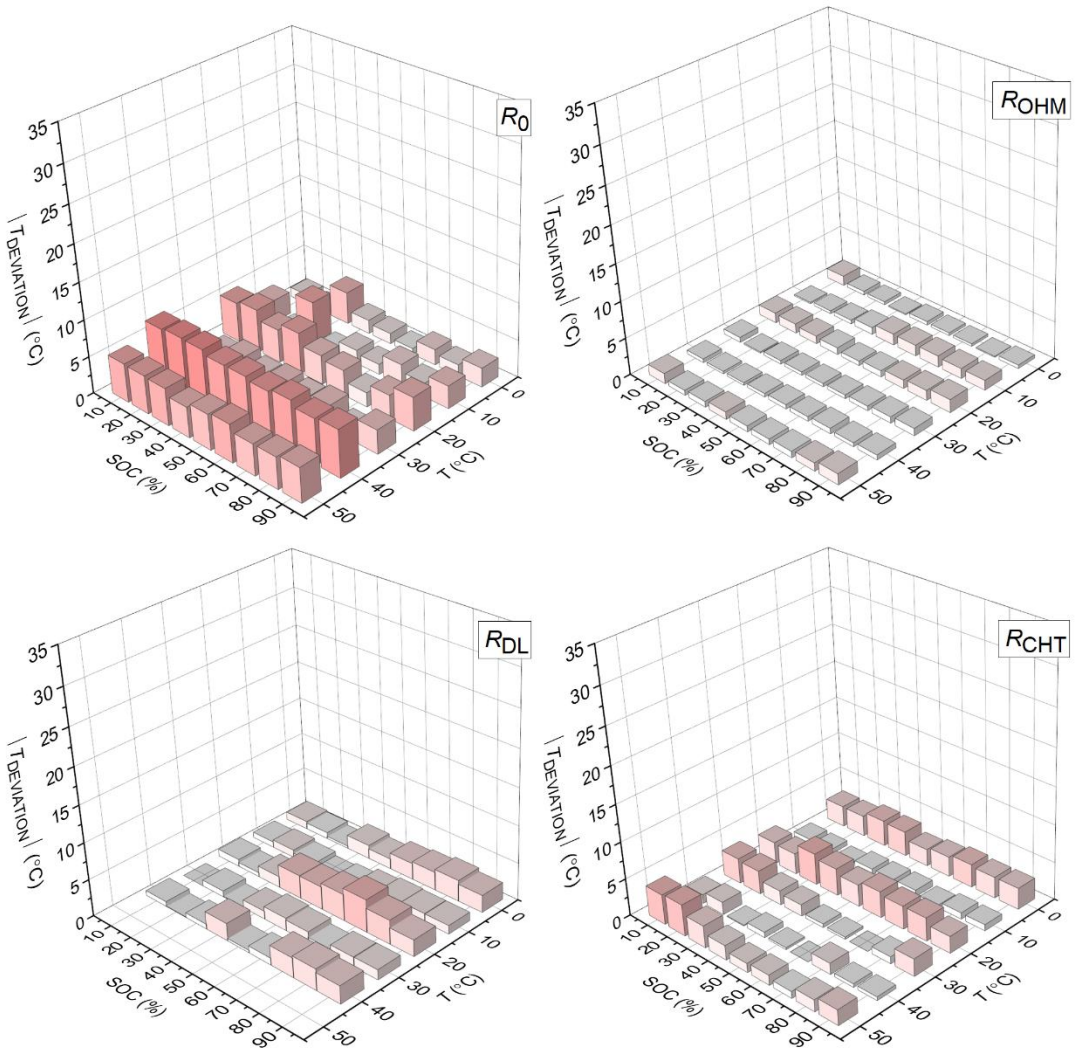


Figure 4.4: *Temperature deviation for selected ECM parameters.*

Temperature Dependence of DRT Features

DRT analysis identified four main peaks, corresponding to the main features observed in the Nyquist plots. Peak A was associated with high-frequency electric or electromagnetic properties of the current collectors. Peak B corresponded to double-layer processes, Peak C to charge-transfer processes and Peak D to lithium-ion diffusion.

All DRT peaks generally increased in magnitude with decreasing temperature, while some peaks also shifted in relaxation time. However, not all peaks were suitable for internal temperature determination. Peak B was not sufficiently consistent and disappeared under some conditions, similarly to the RDL feature in the ECM analysis. Peak C also showed insufficient accuracy, especially at lower temperatures and lower SOC levels. Peak D showed promising accuracy across the full SOC range. However, it is associated with low-frequency diffusion processes, meaning that the EIS measurement required to obtain this feature is time-consuming. In practical applications, such long measurement times are problematic because

the battery temperature may change during the measurement itself. In addition, diffusion-related features can be affected by structural degradation of active materials, which may reduce their reliability as temperature indicators. Peak A was identified as the most practically suitable DRT feature. Although its best accuracy was achieved mainly at SOC values above 50%, it has several important advantages. It is obtained from the high-frequency part of the impedance spectrum, which can be measured within tens of seconds. Therefore, it is much less affected by temperature drift during the measurement. Moreover, since Peak A is associated with the electric or electromagnetic properties of current collectors, it is expected to be less sensitive to typical electrochemical degradation mechanisms than ECM parameters or diffusion-related DRT features. Taking these factors into account, Peak A represents the most suitable feature for determining the internal temperature of the studied EV battery module, particularly for SOC values above 50%.

4.2. Influence of thermal stabilisation on EIS-based state-of-health diagnostics

The main motivation of this work was to investigate whether stabilisation of the module casing temperature (Figure 4.5) is sufficient to ensure reliable EIS measurements. This is particularly relevant for second-life battery testing, where modules may be moved from storage facilities to testing lines with different ambient temperatures. Due to the large thermal mass of EV battery modules, the casing temperature may stabilise earlier than the internal electrochemical processes.

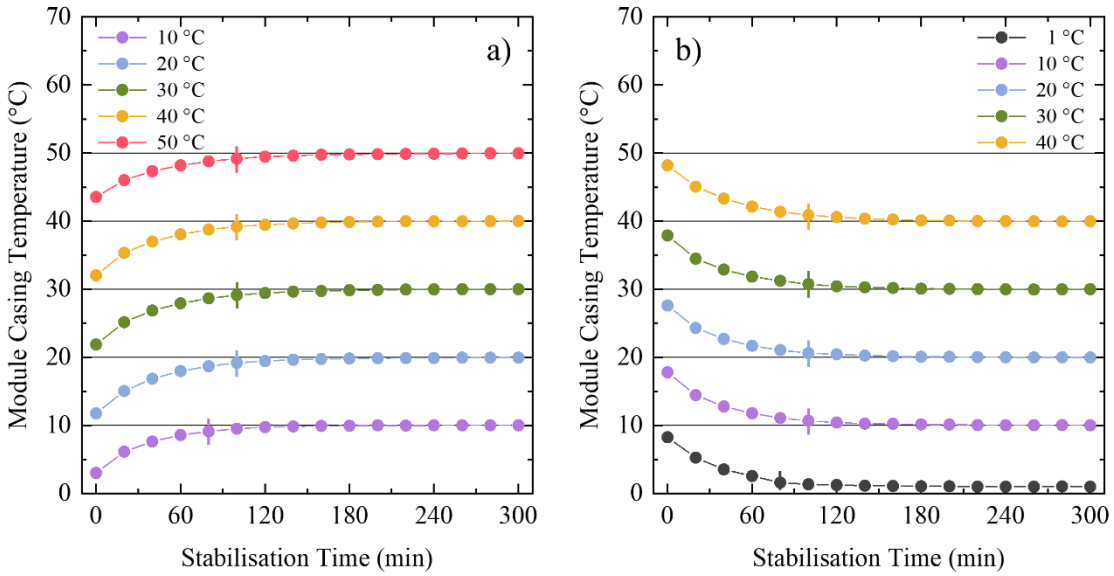


Figure 4.5: *Module casing temperature stabilisation after a) heating and after b) cooling.*

The identical Nissan Leaf battery module was used in the experiment as in the previous work. The module was placed in a climate chamber and subjected to step changes in ambient temperature from 1 °C to 50 °C and then back down. At each temperature step, EIS measurements were repeatedly performed for 5 hours. The module casing temperature was

continuously monitored using a PT100 sensor. The results showed that the module casing required approximately 100 minutes to stabilise after a 10 °C change in ambient temperature. However, the EIS spectra continued to evolve even after the casing temperature appeared stable. This demonstrates that the stabilisation of the casing temperature does not necessarily mean that the internal temperature and electrochemical processes inside the module are fully stabilised.

The EIS data were fitted using an equivalent circuit model consisting of ohmic resistance, SEI resistance, charge-transfer resistance, and a Warburg diffusion element. The relative errors of these parameters were evaluated after the casing reached thermal stability and compared with a 2% benchmark, representing the accuracy level commonly reported in recent EIS-based SOH estimation studies (Figure 4.6). This comparison showed that EIS measurements performed before thermal stabilisation of the module casing differed substantially from those obtained after stabilisation. Although this behaviour is expected, the results clearly demonstrate that using EIS for SOH evaluation without monitoring the surface temperature of the battery module may lead to significant errors. Moreover, even after 100 minutes, when the casing was considered thermally stabilised, some ECM parameters still exhibited considerable relative changes, limiting their reliability for accurate SOH diagnostics.

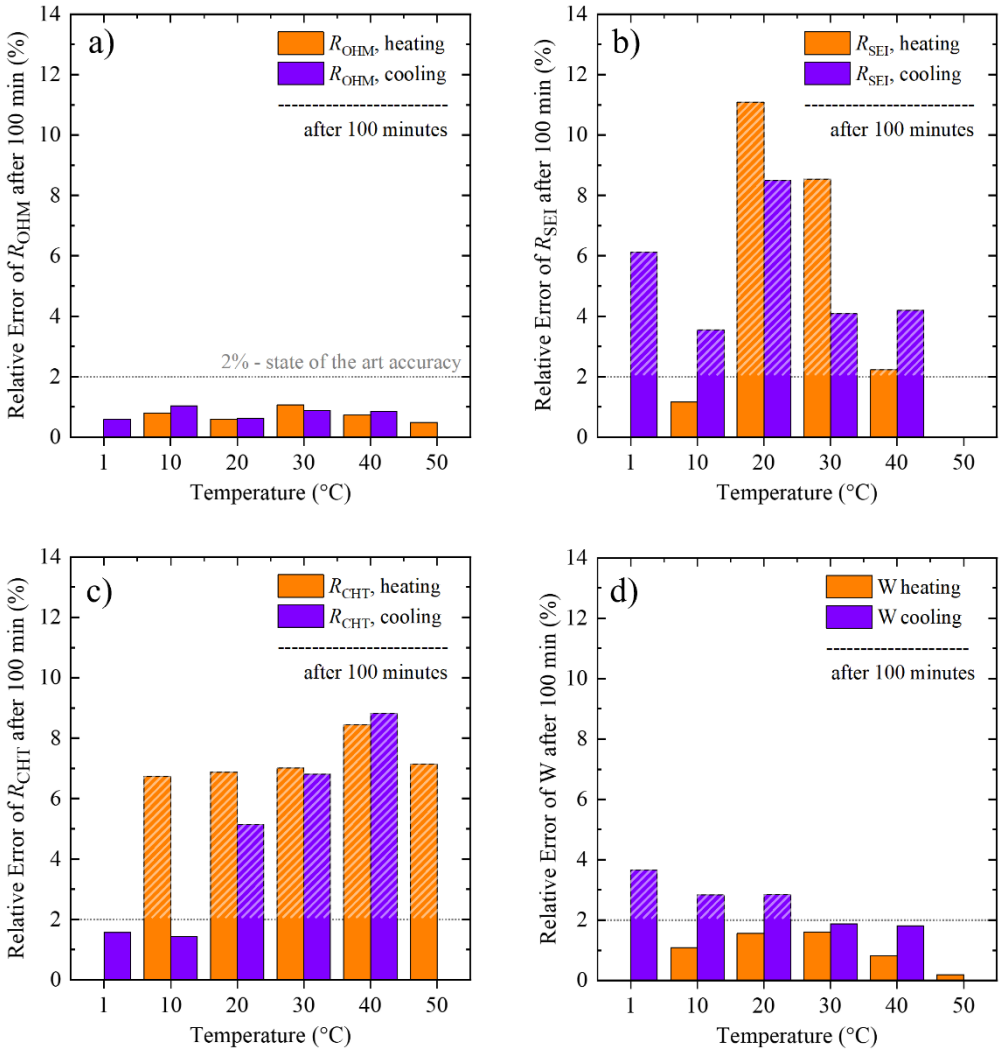


Figure 4.6: *Relative error of individual ECM parameters after the thermal stability of the battery module casing is reached (100 minutes), for (a) R_{OHM}, (b) R_{SEI}, (c) R_{CHT}, (d) W.*

Among the evaluated parameters, ROHM showed the lowest error after casing temperature stabilisation, remaining well below the 2% benchmark. To account for deviations across all temperatures during both heating and cooling, the Relative Root Mean Squared Error (RRMSE) was calculated, yielding 0.79% for ROHM. This indicates that ohmic resistance is the most robust parameter and can be reliably used for SOH evaluation once the casing temperature is stable.

In contrast, RSEI and RCHT showed substantially higher errors, with RRMSE values of 6.31% and 6.48%, respectively. At certain temperatures, the relative error reached 11.09% for RSEI after heating at 20 °C and 8.45% for RCHT after heating at 40 °C. These results indicate that, despite apparent casing stabilisation, the thermal dynamics of SEI-related and charge-transfer processes continue to affect the impedance response. Therefore, the otherwise valuable RSEI and RCHT parameters cannot be reliably used for SOH evaluation immediately after casing

temperature stabilisation. For these parameters, achieving the 2% benchmark required an additional 80–120 minutes beyond casing temperature stabilisation.

The Warburg impedance, associated with lithium-ion diffusion, showed an RRMSE of 2.08%, placing it close to the 2% benchmark. This suggests that it can be considered potentially usable, particularly at typical testing temperatures around 20–30 °C, although its reliability is still slightly lower than that of ROHM.

4.3. Conclusion

This study investigated the potential of electrochemical impedance spectroscopy (EIS) and distribution of relaxation times (DRT) analysis as non-invasive tools for battery state and safety risk monitoring through internal temperature estimation of a used EV battery module. The results demonstrated that several impedance-derived features exhibit strong temperature dependence and can therefore provide reliable information about the internal thermal state of the battery. Since internal temperature is one of the key parameters governing battery ageing, performance, and safety, accurate EIS-based temperature estimation can significantly improve thermal management and early identification of abnormal operating conditions.

The results also demonstrate that relying solely on surface temperature measurements may lead to misleading interpretation of the electrochemical state of the battery. Although the module casing may appear thermally stabilised, internal electrochemical processes associated with the solid electrolyte interphase (SEI) and charge-transfer reactions may still be evolving. This is particularly important because impedance features such as RSEI and RCHT are widely used as indicators of battery ageing and State of Health (SoH). Consequently, accurate knowledge of the internal temperature is essential not only for thermal monitoring itself but also for reliable EIS-based diagnostics, preventing incorrect assessment of battery condition and reducing the risk of misinterpreting safety-critical changes.

Among the evaluated equivalent circuit model (ECM) parameters, ROHM and RCHT showed the highest sensitivity to temperature. However, their practical implementation is limited by their dependence on battery ageing and degradation, requiring extensive calibration across different State-of-Health conditions. Furthermore, ROHM proved to be the most robust parameter under changing thermal conditions, whereas RSEI and RCHT require sufficient thermal stabilisation before they can provide reliable diagnostic information. In contrast, DRT analysis proved to be a more robust approach. Although the low-frequency Peak D exhibited excellent temperature sensitivity over the full SoC range, its long acquisition time limits its applicability for real-time battery management. The high-frequency DRT Peak A, on the other hand, combines rapid acquisition with clear temperature dependence and is expected to be considerably less affected by common degradation mechanisms.

The results identify the high-frequency DRT Peak A as the most promising feature for non-invasive monitoring of the internal temperature of EV battery modules. Its fast response,

strong temperature sensitivity, and expected robustness make it well suited for integration into next-generation battery management systems. Beyond temperature estimation itself, accurate monitoring of the internal thermal state improves the reliability of EIS-based State-of-Health diagnostics, supports thermal management, enables earlier identification of abnormal thermal behaviour, and contributes to enhanced monitoring of safety-critical operating conditions in both electric vehicle and second-life battery applications. Furthermore, the findings provide practical guidance for the design of EIS-based diagnostic protocols, highlighting the importance of internal thermal equilibrium before interpreting impedance-derived health indicators.

5. AI driven methodology for battery state and safety risks monitoring – internal temperature estimation

The passive safety materials developed in the ENSAMAT project, such as Silicon/Graphite anodes and coated NMC cathodes, are influenced by the thermal characteristics of Generation 3 batteries. However, temperature sensors placed on the battery surface, typically used in Battery Management Systems (BMS), create a measurement gap when compared to the internal temperature.

Research indicates that during standard high-rate operations, the internal temperature of a cell can deviate from the surface measurement by 10°C to 12°C . This disparity is attributed to the low thermal conductivity of the jellyroll and the thermal lag associated with heat transfer to the casing. For Generation 3 chemistries like NMC811, maintaining the core temperature within an optimal range is important for preserving the stability of the Solid Electrolyte Interphase (SEI) and the structural integrity of the cathode. Accurate estimation of these internal states allows the BMS to adjust operation profiles before temperature-induced degradation occurs.

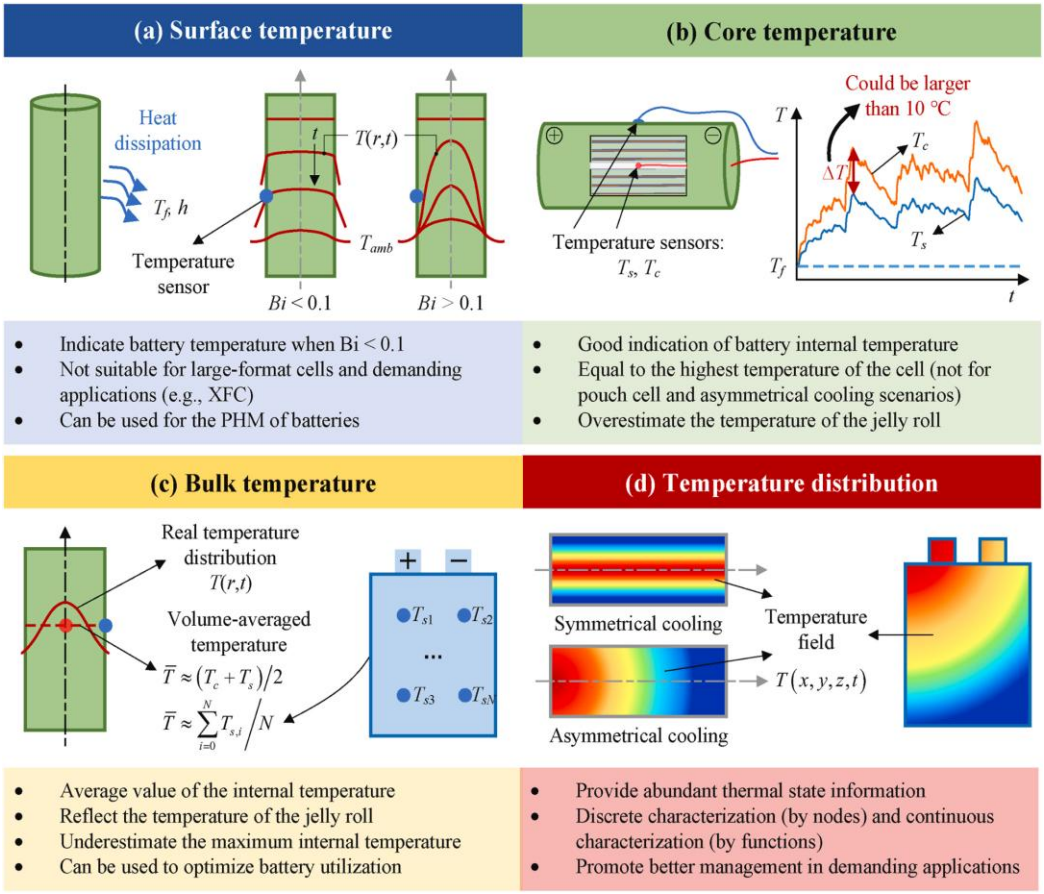


Figure 5.1: *Potential metrics for the characterisation of battery thermal states and their key features. (a) Surface temperature, (b) Core temperature, (c) Bulk temperature, (d) Temperature distribution.*

5.1. Non-Destructive Characterisation via Pulse Response and Impedance

Achieving TRL 3 for this characterisation methodology requires a shift toward non-destructive sensing that can be implemented in a standard electrical environment. This work focuses on the extraction of internal parameters through current pulse responses and operando impedance acquisition.

By analysing the voltage response to a short current pulse (10 ms to 1 s), the DC resistance can be calculated. This parameter serves as a sensitive indicator of the cell's internal thermal state.

For real-time estimation, specific frequencies have been identified that correlate strongly with temperature while remaining largely independent of the State of Charge (SOC). The imaginary part of the impedance at 100 Hz has been proposed as a superior indicator for volume-averaged temperature, offering an accuracy within 0.46°C RMSE.

Beyond temperature, pulse analysis can assist in identifying the onset of lithium plating, an unfavourable state that occurs during high-rate charging or at low temperatures. Monitoring the voltage relaxation curves following a pulse provides a non-invasive way to detect these shifts in internal chemistry.

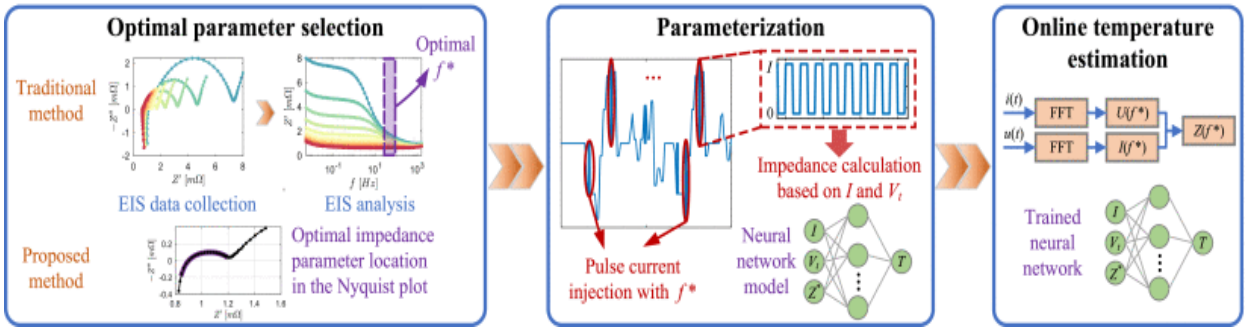


Figure 5.2: *Flowchart of impedance-based battery temperature estimation [8].*

Integrated Estimation Framework: Fusing Physics with Machine Learning

Traditional physical models like the Pseudo-Two-Dimensional (P2D) model provide deep insights but are computationally demanding for onboard BMS. To address this, the project utilises Physics-Informed Neural Networks (PINNs) and hybrid frameworks that combine the accuracy of data-driven methods with the reliability of physical laws.

Unlike "black-box" models, PINNs embed governing thermal equations (Partial Differential Equations) directly into the model's loss function. This ensures that the predictions of internal temperature distribution are physically plausible and thermodynamically consistent.

Hybrid models such as PG-LSTM (Physics-Guided LSTM) or SA-MMPINN (Figure 5.3) can be significantly faster than traditional numerical solvers while maintaining high precision.

As Generation 3 cells age, their internal resistance and thermal parameters shift. By integrating State of Health (SOH) and degradation metrics into the estimation loop, the model remains accurate throughout the battery's entire lifecycle.

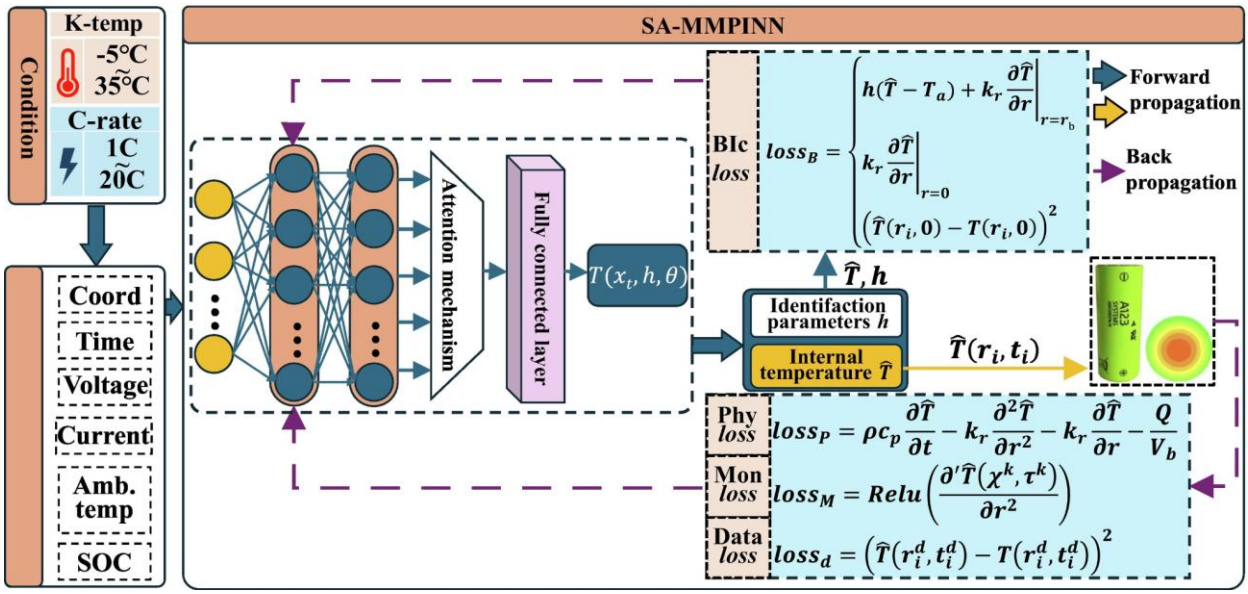


Figure 5.3: *Internal temperature sensing framework for cell.*

Methodology & Experimental procedure

The experimental validation and parameterization of the PINN and FDM thermal models were conducted using commercial Molicel INR21700-P45B cylindrical lithium-ion cells. These 21700 format cells provide a robust empirical baseline for capturing complex thermal dynamics under varying operational stresses.

The initial phases of the PINN development focused on establishing a baseline using Finite Difference Method (FDM) pseudo-labels to supervise core temperature estimation. Key learnings from the early iterations included several areas.

Early single-temperature models failed when exposed to unseen ambient temperatures (e.g., 47.8°C RMSE at 50°C). The training dataset was extended to cover a wide thermal range (0°C to 50°C) to help generalizability.

Raw PDE residuals initially caused gradient explosions. This was mitigated by introducing strict amplitude normalization and adaptive time-sub-stepping to maintain stability during varying protocol gaps.

As battery cells age, more significant in silicon-based cells, their internal resistance and thermal parameters shift. To address this, State of Health (SOH) was integrated as a direct network input alongside SOH-aware Open Circuit Voltage (OCV) calculations. This prevented the systematic underestimation of heat generation in degraded cells, allowing the model to interpolate thermal behaviors across the battery's entire lifecycle.

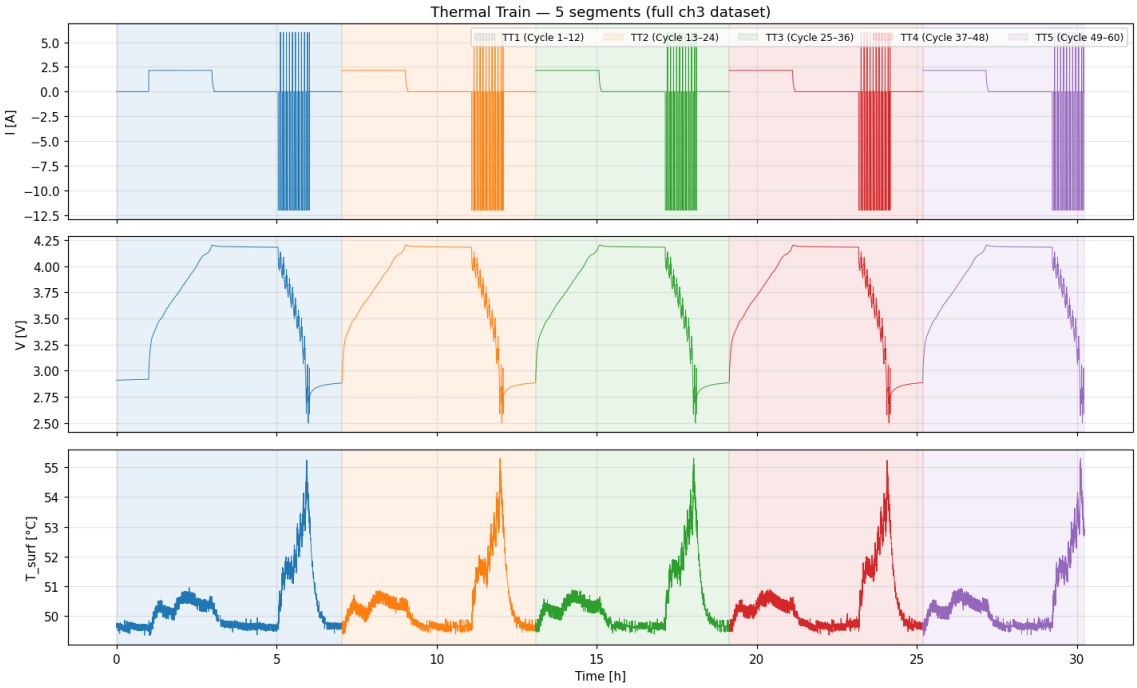


***Figure 5.4**: Experiment procedure used for internal temperature estimation.*

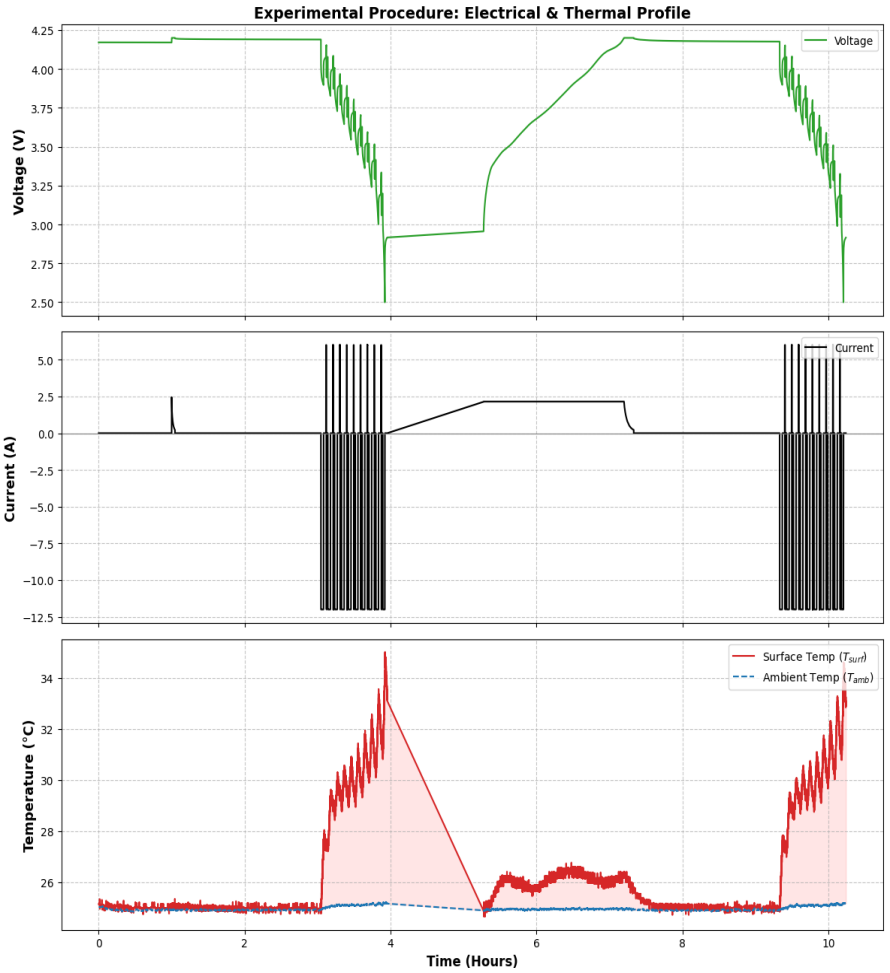


***Figure 5.5**: Detail on experimental procedure and surface temperature vs. ambient temperature over time.*

Physical Calibration and Convection Corrections

Transitioning to testing on actual Thermal Train (TT) segments revealed physical inconsistencies. Specifically, the FDM solver produced physically incorrect cooling curves during rest phases. Diagnostics revealed that the initial heat transfer coefficient (h) was based on natural convection literature values. However, the experimental chamber utilized an active fan. A numerical grid search successfully calibrated the h-coefficient to 51.0 , aligning it with forced convection dynamics and reducing the surface temperature RMSE from 7°C to 0.78°C. The model's accuracy was significantly boosted by replacing theoretical approximations with bilinear interpolation from empirically measured pseudo-OCV curves across varying temperatures.

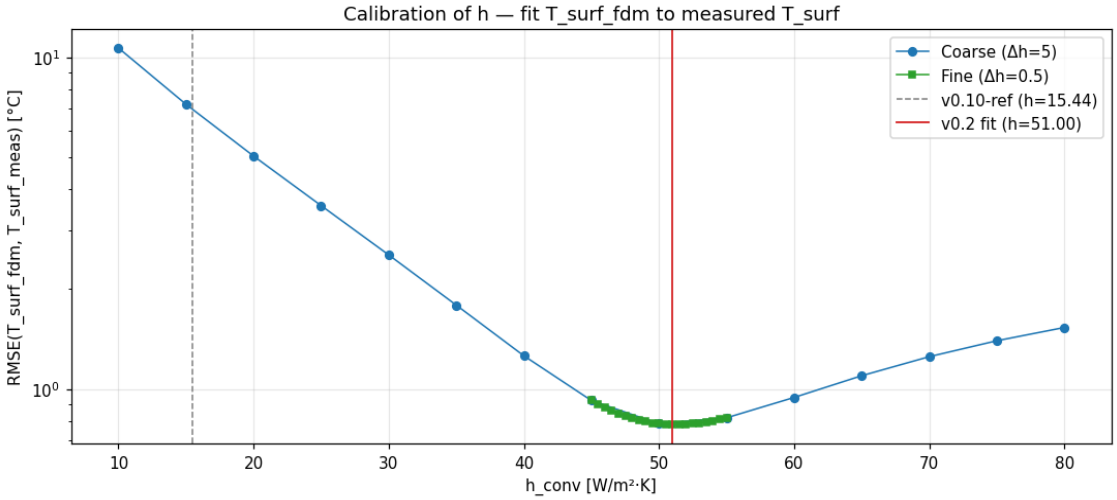


***Figure 5.6**: calibration of heat transfer coefficient for forced convection.*

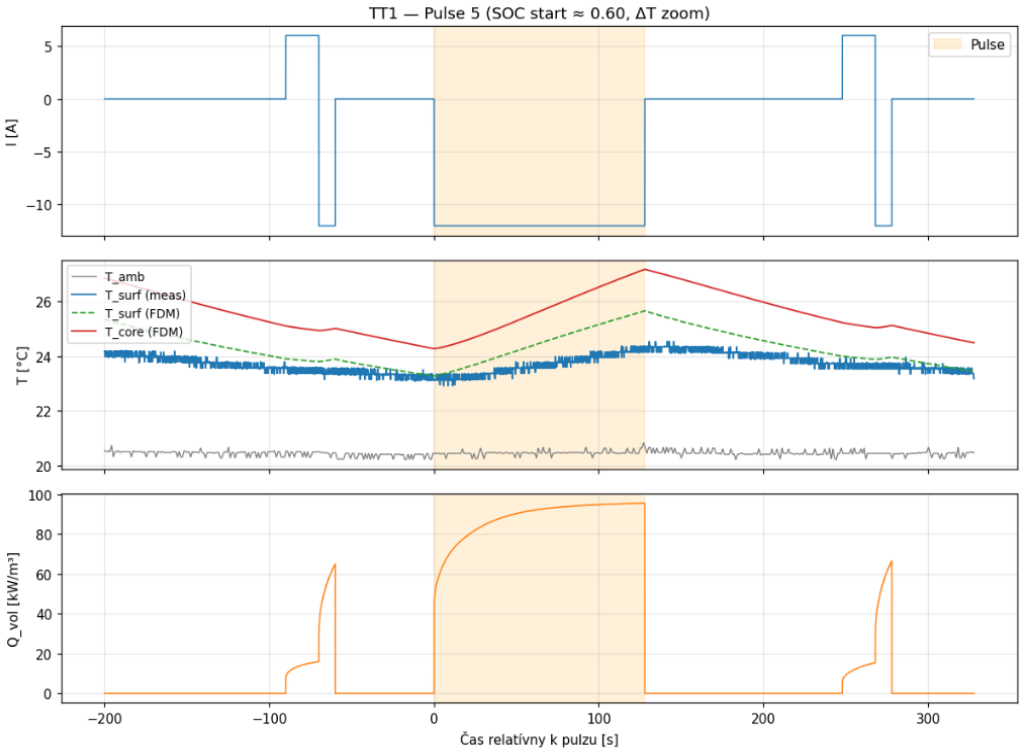


Figure 5.7: *FDM pseudo label calculation over one pulse sweep of the Thermal Train procedure.*

Transition to a "Clean PINN" Framework

Despite improvements, the model remained overly reliant on data-driven inputs (like Q_{vol} flags) and implicit physics, leading to non-physical behavior in low-current regimes (like predicting core temperatures below ambient during rest phases).

New version achieved a major architectural update by implementing a true "Clean PINN". The network was refactored to a single-head $T(r,t)$ model where the radial coordinate (r) acts as a continuous input, moving away from the disconnected dual-head (surface vs. core) approach. FDM pseudo-labels were demoted to a soft prior. Instead, the network strictly enforced the 1D radial heat equation residual and Newton cooling boundary constraints. To ensure the physics losses effectively guided the network without exploding, the heat equation residuals and boundary fluxes were non-dimensionalized against characteristic volumetric heat generation (Q_{vol_char}) and scaling factors.

By embedding strict thermodynamic rules into the neural network architecture, the latest iteration successfully captures the internal core-to-surface thermal lag across all operational phases. The PINN now achieves reliable, physically valid internal estimations even during out-of-distribution tests, directly supporting the project's goal of enabling earlier, sensor-light warnings for thermal runaway prevention.

5.2. Results

The application of the integrated PINN and FDM created an accurate estimations of internal core temperatures for the Molicel INR21700-P45B cylindrical cells across varying operational profiles. Validation successfully tracks complex internal thermal dynamics using solely external measurements specifically voltage, current, and surface temperature. The model maintained a consistently low error margin even under high-stress charging and discharging scenarios.

The incorporation of specific SOH metrics allowed the algorithm to adapt dynamically to cell degradation, ensuring that thermal predictions remain reliable throughout the battery's lifecycle. These results confirm that the proposed AI methodology provides a robust and computationally efficient framework suitable for real-time deployment in advanced Battery Management Systems (BMS). This non-destructive diagnostic approach directly advances the overarching objectives of the project by enabling earlier, more precise detection of safety-critical internal thermal states without the need for complex internal sensing hardware.

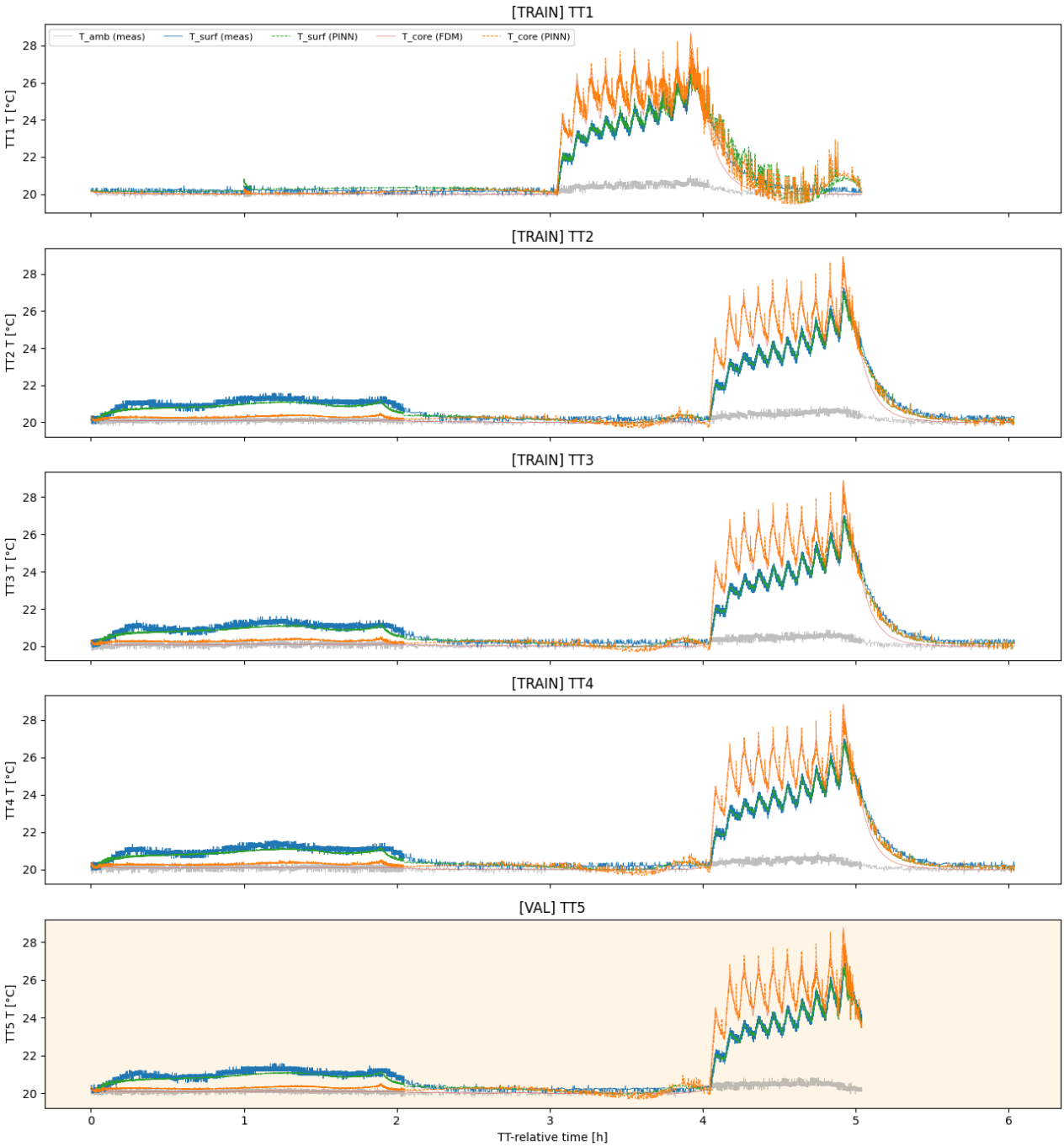


Figure 5.8: *Results of the internal temperature estimation from PINN model.*

Figure 5.9-11 supports the internal/surface temperature gap anticipated from the current state of the art. The radial profiles (Figure 5.4) show a core-to-surface gradient that widens during current pulses and partially recovers during rest, in line with the limited thermal conductivity of the jellyroll. The radial-time field (Figure 5.5) shows how this gradient develops across the whole SOC range, with the core response lagging the surface response. The zoomed view (Figure 5.6) further indicates that the surface-core difference is not constant but scales with pulse magnitude and duration, reinforcing the need for internal-state estimation rather than surface sensing alone.

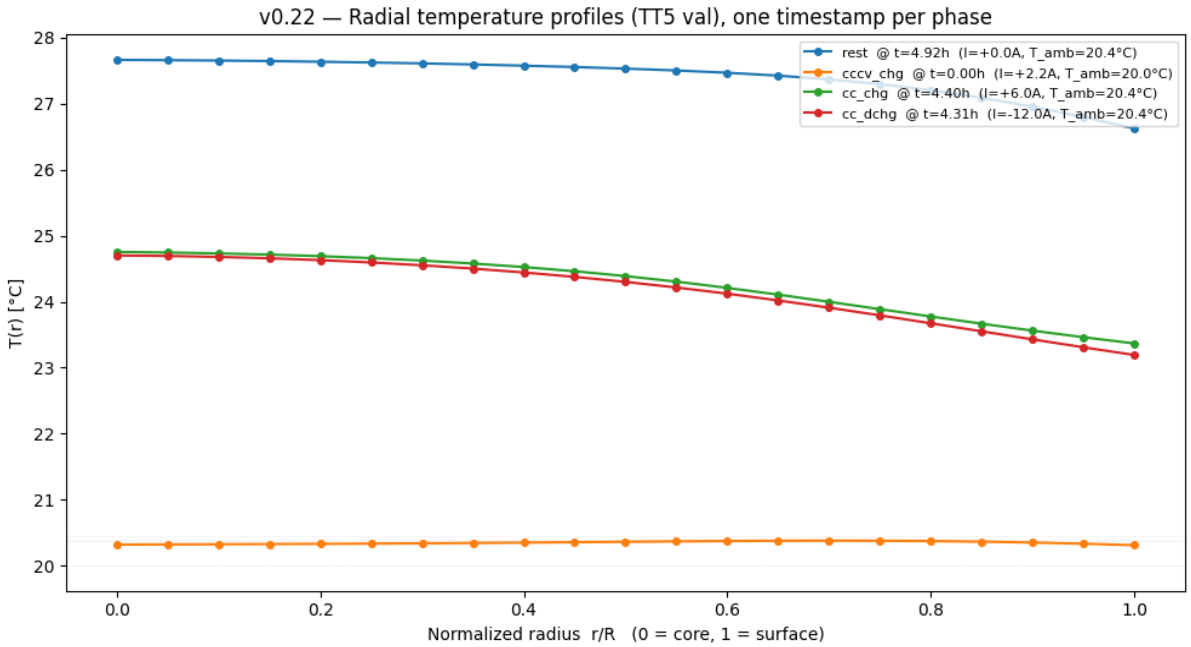


Figure 5.9: *Radial temperature profiles between the core and the surface of the battery cell on the validation subset.*

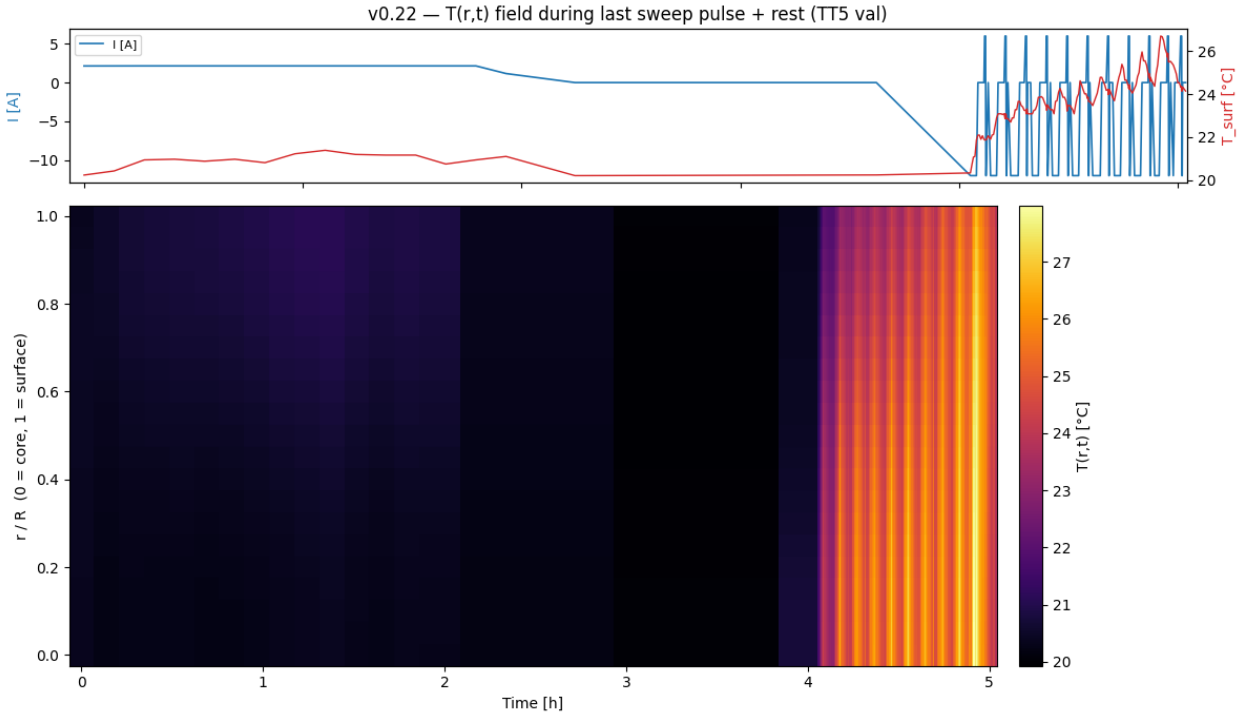


Figure 5.10*: Temperature 2D radial-time field (T(r,t)) during pulses over the whole SOC range, including a rest period on the validation subset.*

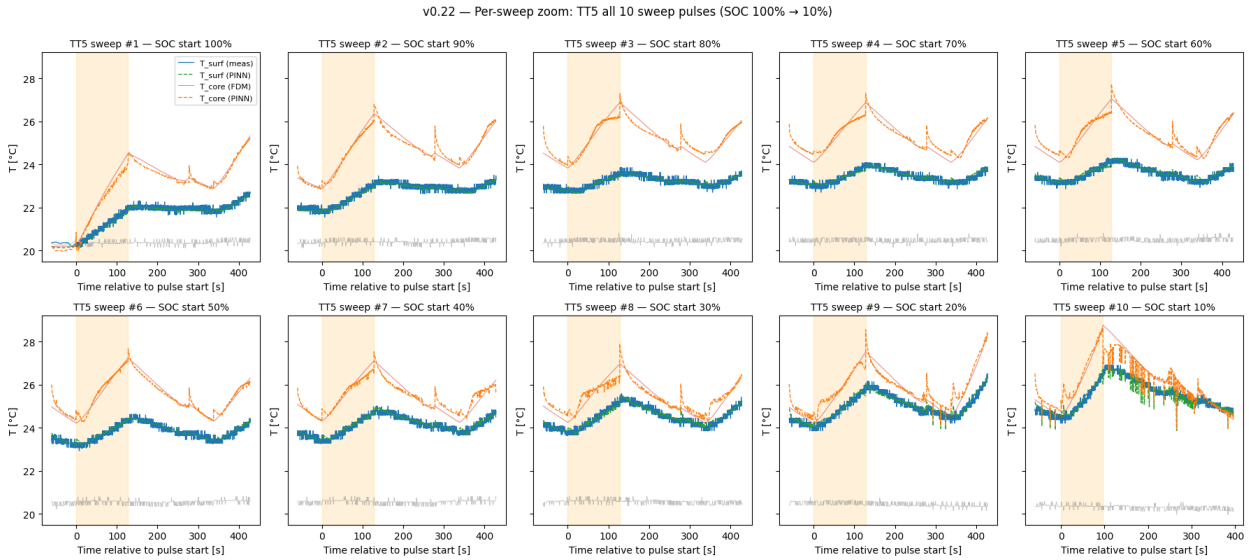


Figure 5.11: *Zoom on partial pulses over the whole SOC-wide discharge and the difference between surface and internal temperature.*

5.3. Conclusion

The development of this characterisation methodology directly supports the ENSAMAT objective of enhancing battery reliability. By providing an accurate, non-invasive method to monitor internal thermal states, this system complements the passive safety of Silicon-modified anodes and coated cathodes. This approach identifies operating conditions which can lead to a thermal runaway event sooner, establishing an enhanced framework for Generation 3 battery management.

Extent of application and relevance: the internal-temperature estimation methodology targets TRL 3 by the end of the project and is intended as a supporting characterisation tool rather than a standalone safety solution. It applies most directly to the prototype cells built around the Si/graphite anode and NMC/LFP cathode materials developed elsewhere in ENSAMAT, giving a non-destructive way to relate anode/cathode coating changes to internal thermal behaviour under abusive cycling. Its main relevance is enabling earlier, sensor-light warning of conditions that prevent thermal runaway, which can complement the passive material-level safety measures with an active, BMS-oriented detection layer. Validation on the separator-integrated prototypes and correlation with post-mortem findings remain open for the next project phase.

6. Summary of results

This report presents a set of complementary non-destructive methodologies developed and experimentally validated for monitoring battery state and safety risks using commercially available lithium-ion cells and battery modules. Rather than relying on a single diagnostic technique, the proposed approach combines acoustic, mechanical, electrochemical and data-driven methodologies to obtain comprehensive information about the internal condition of the battery. Together, these techniques provide complementary insight into electrochemical, thermal, mechanical and structural processes that are directly linked to battery performance, ageing and operational safety.

Ultrasonic defectoscopy demonstrated the capability to estimate both the State of Charge and the internal temperature of lithium-ion cells using independent acoustic signal features. The transmitted amplitude was shown to be primarily sensitive to the electrochemical state, whereas the time-of-flight exhibited strong temperature dependence, enabling simultaneous monitoring of battery state and internal thermal conditions. Furthermore, the correlation between acoustic features and incremental capacity analysis confirmed that ultrasonic measurements reflect underlying electrochemical processes and therefore provide a promising basis for future degradation diagnostics and early detection of abnormal internal conditions.

Surface strain sensing proved to be an effective complementary methodology for monitoring the mechanical response of lithium-ion cells. Numerical electrochemical-mechanical modelling together with experimental measurements showed that strain evolution is influenced by silicon content, State of Charge, operating temperature, current load and ageing. The observed degradation-related changes in strain profiles, together with the sensitivity of strain measurements to local structural imperfections identified by X-ray computed tomography, demonstrate the potential of mechanical sensing for identifying increasing mechanical instability and supporting early warning of safety-relevant degradation mechanisms.

Electrochemical impedance spectroscopy provided a reliable methodology for estimating the internal temperature of used EV battery modules. The study demonstrated that impedance-derived features are strongly temperature dependent and that high-frequency DRT features offer a robust approach for internal temperature estimation with reduced sensitivity to degradation. The results also highlighted the importance of internal thermal equilibrium for reliable EIS-based State-of-Health diagnostics, showing that relying solely on surface temperature measurements may lead to incorrect interpretation of degradation-related impedance features.

The AI-based methodology further demonstrated how advanced data-driven models can complement experimental diagnostics by providing accurate real-time estimation of internal battery temperature using readily available operational data. Such approaches significantly reduce the need for intrusive sensing while supporting continuous monitoring of thermal conditions during battery operation.

Overall, the results demonstrate that battery safety cannot be reliably assessed using a single physical quantity. Electrochemical, thermal, mechanical and structural degradation processes evolve simultaneously and often precede measurable changes in conventional electrical variables. The complementary methodologies presented in this report therefore provide a significantly richer description of battery behaviour than voltage, current and surface temperature measurements alone. Their integration offers a promising framework for future battery management systems capable of more accurate battery state estimation, earlier detection of abnormal operating conditions, improved thermal management and enhanced monitoring of safety-critical phenomena throughout the battery lifetime.

The methodologies developed within this activity establish a methodological foundation for future work in the ENSAMAT project, where they can be applied to advanced battery materials and next-generation cell concepts. Their further integration into multi-sensor diagnostic systems and intelligent Battery Management Systems is expected to contribute to safer, more reliable and longer-lasting lithium-ion batteries for both electric vehicle and stationary energy storage applications.